J. Fluid Mech. (2024), *vol*. 983, A21, doi:10.1017/jfm.2024.122

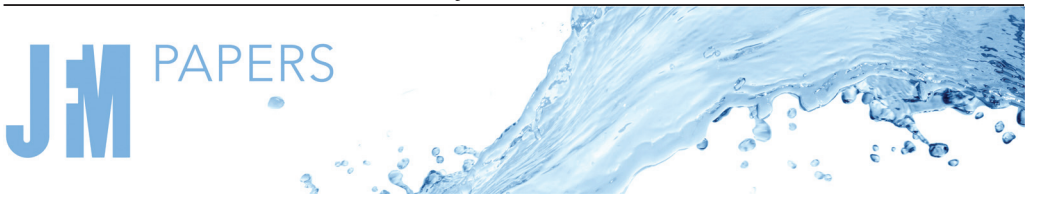

Evaporation of binary liquids from a capillary tube

Lijun Thayyil Raju[1,†], Christian Diddens[1], Javier Rodríguez-Rodríguez[2], Marjolein N. van der Linden[1,3], Xuehua Zhang[1,4], Detlef Lohse[1,5,†] and Uddalok Sen[1,6,†]

[1]Physics of Fluids Group, Max Planck Center Twente for Complex Fluid Dynamics, Department of Science and Technology, and J. M. Burgers Centre for Fluid Dynamics, University of Twente, P. O. Box 217, 7500 AE Enschede, The Netherlands

[2]Departmento de Ingeniería Térmica y de Fluidos, Gregorio Millán Institute for Fluid Dynamics, Nanoscience and Industrial Mathematics, Universidad Carlos III de Madrid, 28911 Leganes, Spain

[3]Canon Production Printing B. V., P.O. Box 101, 5900 MA Venlo, The Netherlands

[4]Department of Chemical and Materials Engineering, University of Alberta, Edmonton T6G1H9, AB, Canada

[5]Max Planck Institute for Dynamics and Self-Organization, Am Fassberg 17, 37077 Göttingen, Germany

[6]Physical Chemistry and Soft Matter, Wageningen University and Research, Stippeneng 4, 6708 WE Wageningen, The Netherlands

(Received 11 November 2022; revised 14 November 2023; accepted 29 January 2024)

Evaporation of multi-component liquid mixtures in confined geometries, such as capillaries, is crucial in applications such as microfluidics, two-phase cooling devices and inkjet printing. Predicting the behaviour of such systems becomes challenging because evaporation triggers complex spatio-temporal changes in the composition of the mixture. These changes in composition, in turn, affect evaporation. In the present work, we study the evaporation of aqueous glycerol solutions contained as a liquid column in a capillary tube. Experiments and direct numerical simulations show three evaporation regimes characterised by different temporal evolutions of the normalised mass transfer rate (or Sherwood number Sh), namely $Sh(\tilde{t}) = 1$, $Sh \sim 1/\sqrt{\tilde{t}}$ and $Sh \sim \exp(-\tilde{t})$, where $\tilde{t}$ is a normalised time. We present a simplistic analytical model that shows that the evaporation dynamics can be expressed by the classical relation $Sh = \exp(\tilde{t})\,\mathrm{erfc}(\sqrt{\tilde{t}})$. For small and medium $\tilde{t}$, this expression results in the first and second of the three observed scaling regimes, respectively. This analytical model is formulated in the limit of pure diffusion

† Email addresses for correspondence: lijuntraju@gmail.com, d.lohse@utwente.nl, uddalok.sen@wur.nl

and when the penetration depth $\delta(t)$ of the diffusion front is much smaller than the length $L(t)$ of the liquid column. When $\delta \approx L$, finite-length effects lead to $Sh \sim \exp(-\tilde{t})$, i.e. the third regime. Finally, we extend our analytical model to incorporate the effect of advection and determine the conditions under which this effect is important. Our results provide fundamental insights into the physics of selective evaporation from a multi-component liquid column.

Key words: coupled diffusion and flow, microscale transport, condensation/evaporation

1. Introduction

Evaporation of multi-component volatile liquids into a gaseous phase is ubiquitous in both biological and industrial processes (Erbil 2012; Lohse & Zhang 2020; Bourouiba 2021; Morris *et al.* 2021; Lohse 2022). A multi-component liquid can consist of multiple solvents, surfactants, polymers, colloids and salts. Evaporation from such systems leads to a plethora of phenomena, such as instabilities (Li *et al.* 2020), phase separation (Tan *et al.* 2016), altering of deposition patterns (Palacios *et al.* 2012), crystallisation (Shahidzadeh-Bonn *et al.* 2008), stratification (Hooiveld *et al.* 2023) and evaporation-driven flows (Deegan *et al.* 1997; Hu & Larson 2006). In addition to the composition of the liquid, geometrical confinement also affects evaporation significantly. The geometrical confinement can be in the form of a droplet (Picknett & Bexon 1977; Lohse & Zhang 2020), a liquid film (Okazaki *et al.* 1974), a porous membrane (Prat 2002), a shallow pit (D'Ambrosio *et al.* 2021) or a capillary (Chauvet *et al.* 2009).

Understanding the evaporation of liquids from capillaries is crucial for applications such as microfluidics (Zimmermann *et al.* 2005; Bacchin, Leng & Salmon 2022), inkjet printing (Lohse 2022; Rump *et al.* 2023), heat pipes (Chen *et al.* 2016), chromatography (Kamp *et al.* 2005) and the measurement of material properties (Roger, Sparr & Wennerström 2018; Merhi *et al.* 2022; Nguyen, Bouchaudy & Salmon 2022). Capillaries are also considered to be idealised systems for modelling porous structures (Yiotis *et al.* 2007; Chauvet *et al.* 2009; Chen *et al.* 2022; Le Dizès Castell *et al.* 2023), the transport of water across skin (Sparr & Wennerström 2000; Roger *et al.* 2016) and film drying (Guerrier *et al.* 1998; Salmon, Doumenc & Guerrier 2017).

Capillary evaporation is determined mainly by the behaviour of the volatile liquid meniscus. There have been several experimental and numerical studies to determine the evaporation from a liquid meniscus. These studies describe the evaporation rate (Wayner & Coccio 1971), heat transfer coefficients (Wayner, Kao & LaCroix 1976; Park & Lee 2003; Dhavaleswarapu, Murthy & Garimella 2012; Zhou *et al.* 2018), shape of the meniscus (Potash & Wayner 1972; Swanson & Herdt 1992), capillary flows that replenish the evaporated liquid (Potash & Wayner 1972; Ransohoff & Radke 1988; Park & Lee 2003) and additional flows that might be driven by evaporation-induced surface tension gradients (Schmidt & Chung 1992; Buffone & Sefiane 2003; Dhavaleswarapu *et al.* 2007; Cecere, Buffone & Savino 2014) or buoyancy (Dhavaleswarapu *et al.* 2007; Buffone 2019).

Broadly speaking, the evaporation of a single-component liquid from a capillary can be divided into two main classes depending on the location of the liquid–air meniscus with respect to the open end of the capillary (henceforth referred to as its 'mouth'; see figure 1*a*). In the first class of problems, the liquid–air interface is far away from the mouth of the capillary. In such a configuration, the evaporation rate is limited by the transport

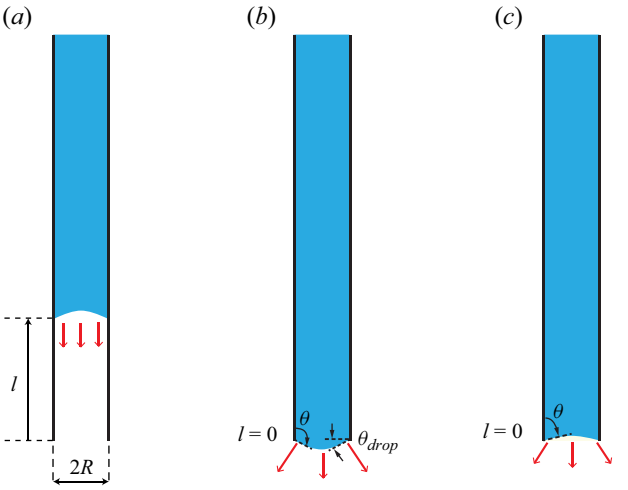

Figure 1. Schematic of the different configurations of evaporation from a capillary: (*a*) first class of problems, where the liquid meniscus is away from the mouth of the capillary ($l \gg 0$); (*b*,*c*) second class of problems, where the liquid meniscus is close to the mouth of the capillary ($l \approx 0$), with (*b*) $\theta > 90^\circ$ and (*c*) $\theta < 90^\circ$. Red arrows represent the evaporative flux.

of vapour from the liquid–air interface to the mouth of the capillary tube, and it varies approximately as the inverse square root of time (Stefan 1873, 1889).

In the second class of problems, the liquid meniscus is at (or relatively close to) the mouth of the capillary (Chauvet *et al.* 2009; Gazzola, Franchi Scarselli & Guerrieri 2009). Within this second class of problems, if the contact angle inside the liquid between the liquid–gas interface and the capillary wall is $\theta \geq 90^\circ$, then one can realise immediately the resemblance to a sessile droplet (figure 1*b*). In such a case, one can use the Popov model (Popov 2005; Li *et al.* 2019) to predict the evaporation rate. For $130^\circ > \theta \geq 90^\circ$ (which is equivalent to a contact angle of $40^\circ > \theta_{drop} \geq 0^\circ$ in the case of a sessile droplet), the evaporation rates will be practically independent of the contact angle (Sobac & Brutin 2011) and depend mainly on the base radius, ambient humidity and properties of the liquid.

However, when $\theta \leq 90^\circ$, the droplet model for evaporation is no longer applicable (figure 1*c*). The evaporation under such conditions shows two distinct regimes – a 'constant rate period' and a 'falling rate period' (Chauvet *et al.* 2009; Keita *et al.* 2014, 2016) – similar to that observed during the drying of a porous medium (Coussot 2000). During the constant rate period, evaporation is still determined mainly by the ambient conditions. To replenish the liquid lost by evaporation, upstream liquid is driven by capillary pressure to the mouth of the capillary through thin liquid films (Ransohoff & Radke 1988; Chauvet, Duru & Prat 2010). However, even during the so-called constant rate period, the evaporation rate decreases slightly (Coussot 2000; Chauvet *et al.* 2009). For square capillaries, this slight decrease is due to the thinning of liquid films at the mouth of the capillary (Chauvet *et al.* 2009). As evaporation proceeds further, the depinning of the liquid films from the mouth of the capillary leads to the falling rate period (Chauvet *et al.* 2009). When the liquid meniscus is sufficiently far away from the mouth of the capillary, the situation reverts to the first class of problems (figure 1*a*).

In addition to the studies on evaporation of single-component liquids from capillaries, there have also been several studies on evaporation in multi-component systems, such as evaporation of binary liquid mixtures (Duursma, Sefiane & Clarke 2008; Cecere *et al.* 2014; Salmon *et al.* 2017; Zhou *et al.* 2018), surfactant solutions (He *et al.* 2015;

Roger *et al.* 2016, 2018), salt solutions (Camassel *et al.* 2005; Naillon *et al.* 2015) and colloidal dispersions (Abkarian, Nunes & Stone 2004; Kamp *et al.* 2005; Sarkar & Tirumkudulu 2009; Wang *et al.* 2020; Roger & Crassous 2021) in capillaries. In all these scenarios, evaporation leads to spatio-temporal variations in the composition of the mixture. Nevertheless, it is generally possible to model the capillary evaporation of a multi-component system as a one-dimensional transport problem. It is unsurprising, but perhaps interesting to note, that in the absence of instabilities (de Gennes 2001), the one-dimensional model of evaporation of polymeric liquid films (Okazaki *et al.* 1974; Guerrier *et al.* 1998; Saure, Wagner & Schlünder 1998; Okuzono, Ozawa & Doi 2006) is mathematically equivalent to the evaporation of binary solutions from capillaries (Salmon *et al.* 2017).

In multi-component systems, especially binary systems, the evaporation rate can also show a constant rate period followed by a falling rate period (Okazaki *et al.* 1974; Salmon *et al.* 2017; Huisman *et al.* 2023), similar to pure liquids. However, in multi-component systems, the different evaporation regimes are determined additionally by changes in the composition of the mixture. Hence a complete evaporation model must include the spatio-temporal variations in the composition and properties of the mixture. Recently, Salmon *et al.* (2017) showed how a steep decrease in thermodynamic activity and the diffusion coefficient of water at high solute concentrations can lead to evaporation being almost independent of ambient humidity for certain molecularly complex fluids. These authors modelled the variable diffusion coefficient as a piecewise-constant function, but bypassed the necessity of using an analytical expression for the thermodynamic activity of water. Moreover, Salmon *et al.* (2017) considered the parameter range where the medium can be approximated as semi-infinite.

In this work, we study the evaporation of binary liquids in capillaries with experiments, direct numerical simulations and analytical modelling. We perform experiments for the evaporation of water–glycerol mixtures in a cylindrical capillary tube under controlled humidity conditions. Our direct numerical simulations show excellent agreement with the experiments. Further, to unravel the physics of the evaporation dynamics, we develop a one-dimensional analytical model. We introduce a linear approximation for the thermodynamic activity of water as a function of its weight fraction. We also identify the condition under which the semi-infinite assumption breaks down and accordingly take it into account in our modelling. Finally, we discuss the explicit role of the advective mass transport compared with the diffusive mass transfer for our particular system. We show that our model predicts accurately the relevant scaling laws observed in the experiments and the numerical simulations.

The paper is organised as follows. In § 2, we describe the experimental set-up and observations. The governing equations of our system and the numerical method are described in § 3. In § 4, we provide three simplified analytical models of the problem, each with an added level of complexity over its predecessor, and compare their predictions with the results obtained from the experiments and the simulations. The paper culminates in a summary of the results and an outlook in § 5.

2. Experiments

2.1. *Experimental set-up*

Aqueous solutions of different mass fractions of glycerol (Sigma-Aldrich) were used as the probe liquids in the present experiments. The use of glycerol has the following advantages. First, since glycerol has a very low vapour pressure, it is practically non-volatile under

the current experimental conditions. Thus we need only account for the evaporation of water. Further, since the more volatile liquid (water) has higher surface tension, its evaporation should not lead to any flow instabilities close to the interface (Diddens 2017). Such instabilities occur whenever the mass transfer (evaporation or condensation) leads to an increase in surface tension, such as for evaporating water–ethanol mixtures (Christy, Hamamoto & Sefiane 2011; Bennacer & Sefiane 2014; Diddens *et al.* 2017; Lopez de la Cruz *et al.* 2021) or condensation of water onto a water–glycerol droplet (Shin, Jacobi & Stone 2016; Diddens 2017). A more detailed explanation of such instabilities can be found in Diddens (2017).

In the present experiments, we study the evaporation dynamics of aqueous solutions of glycerol in a thin cylindrical capillary tube (figure 2; inner diameter 1 mm, outer diameter 1.2 mm, length 100 mm; Round Boro Tubing, CM Scientific). The liquid column inside the capillary had an initial height of 19 ± 2 mm. The initial weight fraction of water, w_i, in the water–glycerol mixture was varied as 0.2, 0.6, 0.9 and 1.0, to cover a wide range of initial compositions. The lower end of the capillary was placed inside an in-house-developed, optically transparent, humidity-controlled chamber at room temperature. The humidity and temperature inside the chamber were monitored using a temperature–humidity sensor (HIH6121, Honeywell). The relative humidity (H_r) in the chamber was maintained at $H_r = 10 \pm 5\,\%$. The upper end of the capillary tube was exposed to room humidity ($>50\,\%$). The evaporation or condensation of water at the upper meniscus was negligible compared to the evaporation from the bottom. This is because of the relatively large distance between the liquid's upper meniscus and the capillary's upper end (see Appendix A for a detailed discussion).

The contact line of the lower meniscus remained pinned at the lower mouth of the capillary. Thus the loss of water by evaporation from the lower mouth of the capillary leads to a decrease in the length L of the liquid column (figure 2*c*). To study this evaporation process quantitatively, time-lapsed images of the liquid column were captured using a DSLR camera (D750, Nikon) equipped with either a long-distance microscope (Navitar 12×) or a macro lens (50 mm DG Macro D, Sigma), while the capillary tube was back-illuminated with a cold LED light source (Thorlabs). For pure water, the velocity v_y of the upper interface,

$$v_y = \frac{\mathrm{d}y}{\mathrm{d}t} = \frac{1}{\rho_w}\frac{\mathrm{d}M''}{\mathrm{d}t}, \tag{2.1}$$

is a direct measure of the evaporation rate $\mathrm{d}M''/\mathrm{d}t$ of water, where y is the displacement of the top interface, M'' is the mass per unit area and ρ_w is the density of water.

At a later time, the contact line of the lower liquid meniscus eventually depins. At this point, we stop the measurements because v_y is thereafter no longer a correct measure of the evaporation rate. Additionally, as the lower interface moves inwards into the capillary tube after depinning, the evaporation boundary condition at the lower interface also changes (see § 3.1 for details of the boundary conditions).

2.2. *Experimental results*

The discrete data points in figure 3(*a*) denote the experimentally obtained vertical displacement y of the upper interface with time t for different initial weight fractions of water, w_i. Only every fifth data point is plotted in figure 3(*a*) to avoid overcrowding of the plot. The markers represent the mean of at least three independent experimental realisations, while the error bars (denoting $\pm$ one standard deviation) reflect the

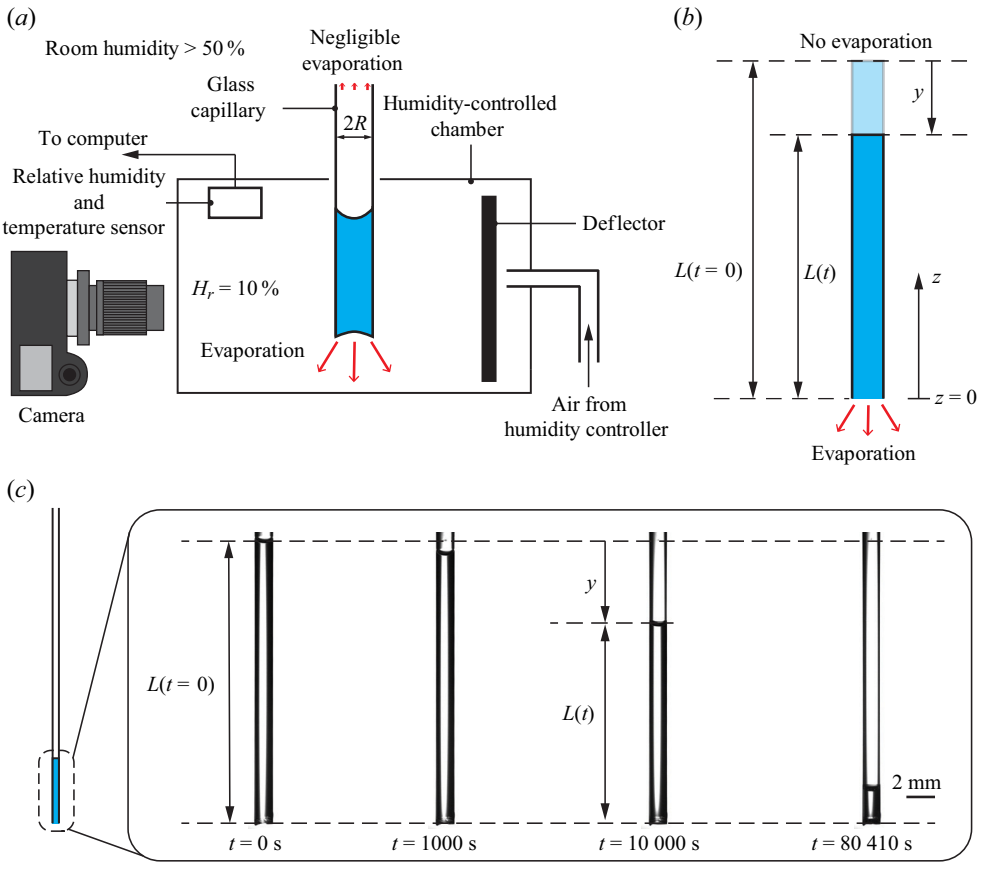

Figure 2. (*a*) Schematic of the experimental set-up. (*b*) Geometry used for numerical simulation and analytical modelling. (*c*) Left: schematic of the relative length of the liquid column with respect to the length of the capillary. Right: time-lapsed experimental snapshots of water–glycerol mixtures in the capillaries for an initial weight fraction of water $w_i = 0.9$. The top interface of the liquid mixture keeps moving downwards due to the evaporation of water from the bottom of the capillary. Red arrows in (*a*,*b*) represent the evaporative flux.

uncertainty due to experimental variabilities and the resolution of the imaging. The velocity $v_y = \mathrm{d}y/\mathrm{d}t$ of the top interface, calculated from y, is plotted as discrete data points in figure 3(*b*).

Obviously, the motion of the top interface depends on the initial composition of the liquid mixture (see figure 3 and supplementary movie 1 available at https://doi.org/10.1017/jfm.2024.122). For pure water ($w_i = 1$), the interface moves at an almost constant velocity ($y = v_y t$ and $v_y(t) \approx 10^{-3}\,\mathrm{mm\,s^{-1}}$; see figure 3). For $w_i = 0.2$ and 0.6, the experiments suggest $y \sim t^{1/2}$ and $v_y \sim t^{-1/2}$ scaling relations. However, for $w_i = 0.9$, the experiments show three different regimes: $v_y(t) \approx 0.8 \times 10^{-3}\,\mathrm{mm\,s^{-1}}$, similar to $w_i = 1$, in approximately the first 800 s; $v_y \sim t^{-1/2}$, similar to $w_i = 0.2$ and 0.6, at intermediate times ($t \lesssim 5 \times 10^4$ s); and a decrease in velocity (which is steeper than $v_y \sim t^{-1/2}$) at long times.

The addition of glycerol reduces primarily the local concentration of water at the lower interface, which in turn leads to a reduced evaporation rate and a decrease in the velocity of the upper interface. Thus we get the so-called constant rate period and the so-called

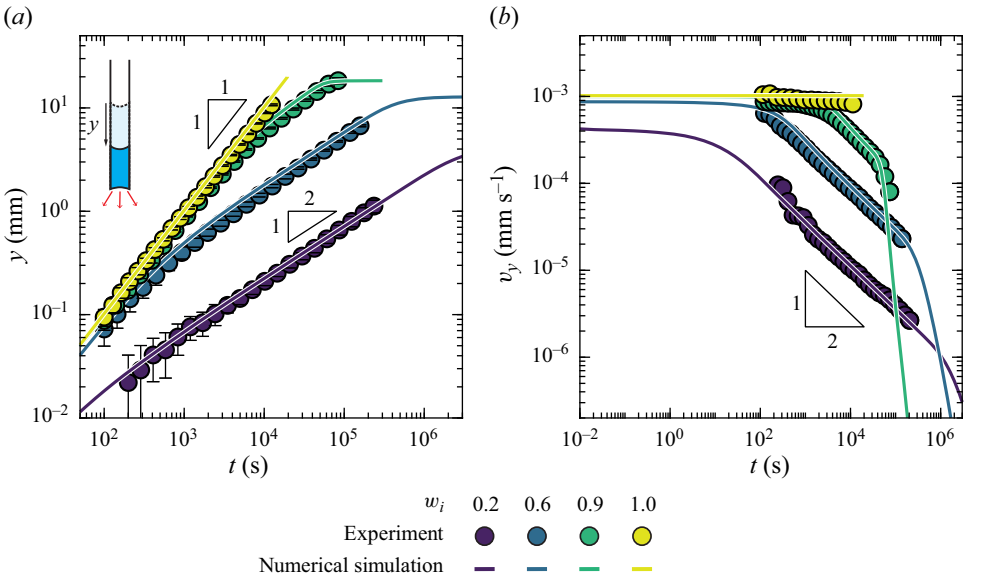

Figure 3. (*a*) Displacement y and (*b*) velocity v_y of the top interface of the aqueous solutions of glycerol observed in experiments (discrete data points) and numerical simulations (continuous lines), for initial weight fractions of water $w_i = 0.2, 0.6, 0.9$ and 1.0.

falling rate period as described in the literature (Salmon *et al.* 2017). Our experimental results, however, raise two important questions. First, why does the constant rate period not appear for $w_i = 0.2$ and 0.6 in the experiments? Second, why does the falling rate period show two sub-regimes for $w_i = 0.9$? To answer these questions, and to understand how the evaporation dynamics of a water–glycerol mixture in a capillary changes with time and the initial composition of the mixture, we develop a theoretical model in the next section.

3. Problem formulation

3.1. *Theoretical model*

We model the column of water–glycerol mixture as a one-dimensional isothermal system with length $L(t)$ (figure 2*b*). The lower end of the capillary is located at $z = 0$. We can express the liquid composition using the weight fraction of water $w(z, t)$; the weight fraction of glycerol then is simply $1 - w(z, t)$. The spatio-temporal variations in the concentration of water in the liquid column can be determined by solving the one-dimensional continuity and advection–diffusion equations:

$$\frac{\partial \rho}{\partial t} + \frac{\partial}{\partial z}(\rho u) = 0 \tag{3.1}$$

and

$$\frac{\partial}{\partial t}(\rho w) + u\,\frac{\partial}{\partial z}(\rho w) = \frac{\partial}{\partial z}\left(\rho D\,\frac{\partial w}{\partial z}\right), \tag{3.2}$$

where $\rho(w)$ is the local density of the mixture, $D(w)$ is the diffusion coefficient of the water–glycerol mixture and u is the fluid velocity along the z-direction.

Initially (at $t = 0$), the composition in the liquid column is uniform and equal to w_i. Since the evaporation of water from the upper interface is negligible (see Appendix A), we model the upper interface as non-evaporative. The lower interface of the liquid column is exposed to the ambient constant relative humidity H_r and loses water by evaporation (per unit area) at rate $\mathrm{d}M''/\mathrm{d}t$. The water lost due to evaporation is replenished by the diffusive and advective transport of water from the bulk liquid inside the capillary. These considerations lead to one initial and two boundary conditions, as follows:

$$\left.\begin{aligned} w &= w_i \quad \text{at } t = 0, \\ \frac{\partial w}{\partial z} &= 0 \quad \text{at } z = L(t), \\ -\rho u w + \rho D \frac{\partial w}{\partial z} &= \frac{\mathrm{d}M''}{\mathrm{d}t} \quad \text{at } z = 0. \end{aligned}\right\} \tag{3.3}$$

The evaporation of water from the bottom interface can be approximated using a quasi-steady diffusion-limited model of evaporation of a pinned sessile droplet having zero contact angle (Popov 2005; Stauber *et al.* 2014):

$$\frac{\mathrm{d}M''}{\mathrm{d}t} = \pi D_{v,a} R (c_{w,s} - c_{w,\infty}) f(\theta_{drop}) \frac{1}{\pi R^2}, \tag{3.4}$$

where $D_{v,a}$ is the diffusion coefficient of water vapour in air, R is the inner radius of the capillary tube, $c_{w,s}$ is the concentration (vapour mass per volume) of water vapour in the air at the lower interface, $c_{w,\infty} = H_r c^o_{w,s}$ is the concentration of water vapour in the ambient air (far away from the capillary), $c^o_{w,s}$ is the saturation concentration of water vapour at the surface of pure water, θ_{drop} is the angle between the horizontal plane and the liquid–air interface at the contact line, and $f(\theta_{drop})$ is a known function of θ_{drop}. For $\theta_{drop} = 0$ as in our model here, $f(\theta_{drop}) = 4/\pi$ (Popov 2005; Stauber *et al.* 2014). Thus

$$\frac{\mathrm{d}M''}{\mathrm{d}t} = \frac{4 D_{v,a}}{\pi R} (c_{w,s} - c_{w,\infty}). \tag{3.5}$$

Here, $c_{w,s}$ depends on the composition of the liquid mixture close to the interface (at $z = 0^+$) and is given by Raoult's law as

$$c_{w,s} = a c^o_{w,s} = x_o \psi_o c^o_{w,s}, \tag{3.6}$$

where $a(w)$ is the thermodynamic activity of water, x_o is the mole fraction of water in the liquid at $z = 0^+$ and $\psi_o(x_o)$ is the activity coefficient of water corresponding to x_o. As long as $c_{w,s} > c_{w,\infty}$, water will evaporate from the lower interface.

3.2. *Numerical solution*

We solve numerically the equations pertaining to the aforementioned one-dimensional theoretical model using finite element method simulations with initial length $L = 20$ mm to obtain the evaporation rates and the spatio-temporal distribution of the concentration of water, w, in the capillary. To that end, a line mesh initially consisting of 100 second-order Lagrangian elements is created to cover the initial length L. The motion of the top interface is realised by moving the mesh nodes along with the top interface, i.e. by an arbitrary Lagrangian–Eulerian (ALE) method with a Laplace-smoothed mesh. The mesh

displacement at the top interface $z = L(t)$, i.e. $\dot{L}(t) = u(L, t)$, is enforced by a Lagrange multiplier acting on the node position at the top. Likewise, the evaporation at the bottom is considered, but here the Lagrange multiplier is acting on the velocity u at $z = 0$, whereas the bottom node remains fixed at $z = 0$.

The implementation of (3.2) and (3.1) along with the boundary conditions (3.3) and (3.5) is achieved by the conventional weak formulations of advection–diffusion equations, including the ALE corrections for the time derivatives. *A posteriori* spatial adaptivity based on the jumps in the slopes of w across the elements is considered. Also, *a posteriori* temporal adaptivity is considered by calculating the difference between the freshly calculated value of each field at each point and its prediction. For the prediction, values from the previous time steps are extrapolated to the current time. If the difference is large, then this means that the system changes excessively during a time step. In that case, the current time step is rejected and calculations are done again with a smaller time step. The implementation has been done with the finite element library OOMPH-LIB by Heil & Hazel (2006), which solves monolithically the coupled equations with a backward differentiation formula of second order for the temporal integration.

The variation of the diffusion coefficient D as a function of the local composition w is considered in the simulations based on the experimental data of D'Errico *et al.* (2004), while the mass density ρ was fitted according to the data of Takamura, Fischer & Morrow (2012). The activity coefficient of water was calculated by AIOMFAC (Zuend *et al.* 2011).

The results of the direct numerical simulations are shown by the continuous lines in figure 3. Excellent agreement between the experiments and the numerical simulations is observed. In particular, figure 3(*b*) shows that the simulations can reproduce the experimentally observed $v_y \sim t^{-1/2}$ scaling for $w_i = 0.2$ and 0.6, and all three velocity scalings for $w_i = 0.9$. Interestingly, the simulations also show that for very early times, v_y is almost constant for $w_i = 0.2$ and 0.6 as well. However, we cannot access these time scales in experiments because of limitations arising from the lack of spatio-temporal resolution. Overall, the quantitative match between experiments and numerical simulations shows that our theoretical model incorporates all the relevant physics of the problem. In figure 10 of Appendix B, we also show the spatial variation in the axial concentration profiles for the different initial concentrations w_i. In the next section, we will use additional simplifying assumptions to formulate a simplistic model that captures the essential physics of the system and recovers the various evaporation regimes.

4. Analytical model

We present here a simplified description of the problem with the purpose of elucidating the physical mechanisms behind the different regimes observed in the experiments and the direct numerical simulations. We introduce some assumptions that will allow us to treat the resulting problem analytically. As we will show below, despite these simplifications, the quantitative comparison between the model and the experiments and simulations is reasonably good. Our one-dimensional analytical model relies on the following assumptions.

(i) Constant properties: we assume that the properties of the water–glycerol mixture, namely the density ρ and diffusion coefficient D, are constant and equal to the values corresponding to the initial composition. These properties can be obtained from figure 12 in Appendix D by setting $w = w_i$. Setting the density to a constant in the continuity equation (3.1) yields that u is independent of z and depends only on t.

Hence

$$u(z,t) = -v_y(t). \tag{4.1}$$

(ii) Linearisation of the water vapour concentration difference: the concentration of water vapour at the liquid–gas interface depends on the concentration of water at $z = 0^+$ in (3.6). To solve the model analytically, we linearise the expression in (3.5) for the difference in concentration of the water vapour between $c_{w,s}(w_i)$ and $c_{w,s}(w_{eq})$ in terms of w:

$$c_{w,s} - c_{w,\infty} = c^0_{w,s}\,\frac{x_i\psi_i - H_r}{w_i - w_{eq}}\,(w|_{z=0} - w_{eq}), \tag{4.2}$$

where x_i, ψ_i and w_i are the initial mole fraction, activity coefficient and weight fraction of water in the liquid mixture, respectively, and w_{eq} is the weight fraction of water at equilibrium, i.e. when $c_{w,s}$ becomes equal to $c_{w,\infty}$ and evaporation stops. In (4.2), we have effectively linearised $c_{w,s} - c_{w,\infty}$ in terms of w, between the initial ($w = w_i$) and final ($w = w_{eq}$) concentrations of water (see detailed derivation in Appendix C). Combining (3.5) and (4.2), we get

$$\frac{\mathrm{d}M''}{\mathrm{d}t} = h^*(w|_{z=0} - w_{eq}), \tag{4.3}$$

where h^*, defined as

$$h^* = \frac{4D_{v,a}c^0_{w,s}}{\pi R\,\Delta w_i}\,(x_i\psi_i - H_r), \tag{4.4}$$

is a modified mass transfer coefficient, with $\Delta w_i = w_i - w_{eq}$. We put an asterisk in h^* to indicate that its units (kg m^{-2} s) are different from those of the conventional mass transfer coefficient h (Incropera *et al.* 2007), which is related to h^* through $h = h^*/\rho$ (unit m s^{-1}).

(iii) Velocity of meniscus: assuming that the volume of the water–glycerol mixture is the sum of the glycerol and water volumes, the velocity at which the length of the liquid column recedes is given by

$$v_y = -\frac{\mathrm{d}}{\mathrm{d}t}\int_0^L \frac{\rho w}{\rho_w}\,\mathrm{d}z, \tag{4.5}$$

i.e. the negative of the time derivative of the volume occupied by the water, since the glycerol volume is constant. Since $\mathrm{d}M''/\mathrm{d}t$ denotes the rate at which the water mass per unit cross-section of capillary is lost, we get

$$v_y = \frac{1}{\rho_w}\frac{\mathrm{d}M''}{\mathrm{d}t}. \tag{4.6}$$

Note that this equation is identical to the exact expression (2.1) obtained for the case where the liquid contains just water. This is a direct consequence of the nearly ideal character of the water–glycerol mixtures.

We define a diffusive length scale l_D (as also done by Salmon *et al.* 2017) based on the mass transfer coefficient by considering a balance between evaporation and diffusion at

the lower interface ($D\,\Delta w/l_D \sim h\,\Delta w$; (3.3) and (4.3)), yielding

$$l_D = \frac{D}{h}. \tag{4.7}$$

Based on the aforementioned considerations, we non-dimensionalise the variables as follows:

$$\tilde{w} = \frac{w_i - w}{w_i - w_{eq}} = \frac{w_i - w}{\Delta w_i}, \quad \tilde{t} = \frac{t}{l_D^2/D} = \frac{h^2\,t}{D}, \quad \tilde{z} = \frac{z}{l_D} = \frac{h\,z}{D}, \quad \tilde{L} = \frac{L}{l_D} = \frac{h\,L}{D}. \tag{4.8a–d}$$

Further, since the velocity of the interface is in fact a proxy for the mass transfer (evaporation) rate of water, as follows from mass conservation, we can describe the system in terms of the Sherwood number, *Sh*. This parameter denotes the non-dimensional velocity or non-dimensional mass transfer rate:

$$Sh = \frac{\rho_w v_y}{h^*\,\Delta w_i}. \tag{4.9}$$

Substituting (4.1)–(4.9) into the governing differential equations (3.1) and (3.2) of mass transport in the capillary, the initial and boundary conditions (3.3), and the equation governing evaporation of water into air (3.5), we get the following system of equations and initial and boundary conditions:

$$\frac{\partial \tilde{w}}{\partial \tilde{t}} - \frac{\rho\,\Delta w_i\,Sh}{\rho_w}\frac{\partial \tilde{w}}{\partial \tilde{z}} = \frac{\partial^2 \tilde{w}}{\partial \tilde{z}^2}, \tag{4.10}$$

$$\left.\begin{aligned} \tilde{w} &= 0 \quad \text{at } \tilde{t} = 0, \\ \frac{\partial \tilde{w}}{\partial \tilde{z}} &= 0 \quad \text{at } \tilde{z} = \tilde{L}, \\ \frac{\partial \tilde{w}}{\partial \tilde{z}} - \left(1 - \frac{\rho\,\Delta w_i\,Sh}{\rho_w}\right)\tilde{w} + \left(1 - \frac{\rho w_i\,Sh}{\rho_w}\right) &= 0 \quad \text{at } \tilde{z} = 0, \end{aligned}\right\} \tag{4.11}$$

$$Sh = 1 - \tilde{w}(\tilde{z} = 0, \tilde{t}). \tag{4.12}$$

Finally, for the case of pure water, we do not need to solve the model for the binary mixture, since there is no change in the concentration. The velocity of the interface can then be obtained directly by substituting $w_i = 1$ in (4.3):

$$v_y = \frac{4D_{v,a}}{\pi R \rho_w}\,c^0_{w,s}(1 - H_r), \tag{4.13}$$

which corresponds to $Sh = 1$.

4.1. *Semi-infinite transient diffusion model*

As the zeroth-order simplification, we assume that advection is negligibly small. Further, we approximate the liquid column as a semi-infinite medium. Thus the governing equation

and the initial and boundary conditions ((4.10) and (4.11)) can be reduced to

$$\frac{\partial \tilde{w}}{\partial \tilde{t}} = \frac{\partial^2 \tilde{w}}{\partial \tilde{z}^2}, \tag{4.14}$$

with

$$\left.\begin{aligned} \tilde{w} &= 0 \quad \text{at } \tilde{t} = 0, \\ \frac{\partial \tilde{w}}{\partial \tilde{z}} &= 0 \quad \text{at } \tilde{z} \to \infty, \\ \frac{\partial \tilde{w}}{\partial \tilde{z}} &= \tilde{w} - 1 \quad \text{at } \tilde{z} = 0. \end{aligned}\right\} \tag{4.15}$$

This is a classical transient diffusion problem with mixed boundary conditions, whose solution is given by (Incropera *et al.* 2007)

$$\tilde{w}\left(\tilde{z}, \tilde{t}\right) = \operatorname{erfc}\left(\frac{\tilde{z}}{2\sqrt{\tilde{t}}}\right) - \exp\left(\tilde{t} + \tilde{z}\right) \operatorname{erfc}\left(\frac{\tilde{z}}{2\sqrt{\tilde{t}}} + \sqrt{\tilde{t}}\right). \tag{4.16}$$

The velocity of the top interface can now be evaluated from the evaporation rate of water using (4.9), (4.12) and (4.16) to yield

$$v_y = \frac{h^* \, \Delta w_i}{\rho_w} \exp(\tilde{t}) \operatorname{erfc}\left(\sqrt{\tilde{t}}\right), \tag{4.17}$$

or

$$Sh = \exp(\tilde{t}) \operatorname{erfc}\left(\sqrt{\tilde{t}}\right). \tag{4.18}$$

For $\tilde{t} \to 0$, $Sh \to 1$, whereas for $\tilde{t} \gg 1$, $Sh \approx 1/\sqrt{\pi \tilde{t}}$.

The predictions of the semi-infinite transient diffusion model (4.18) are compared in figure 4 with the experimental measurements (discrete data points) and the numerical simulations (continuous lines). It can be observed that (4.18) predicts correctly the early-time limit $Sh = 1$ for all cases, and $Sh \sim 1/\sqrt{\tilde{t}}$ at intermediate times for $w_i = 0.2$ and 0.6. Moreover, figure 4 also shows that the predicted value of Sh from the model agrees reasonably well with the experiments and the simulations for $w_i = 0.2$ and 0.6. However, (4.18) severely underpredicts Sh for $w_i = 0.9$ until $\tilde{t} \approx 80$. Furthermore, (4.18) also fails to capture the steep decay in Sh seen in the simulations for $w_i = 0.6$ and 0.9 at long times (figures 4*b*,*c*). This calls for a careful re-examination of the assumptions made in the model.

4.2. *Semi-infinite transient diffusion model with advection – asymptotic solution for $\tilde{t} \gg 1$ and approximate solution for all times*

In order to improve the agreement of our model with the experiments and full numerical simulations, we turn our attention to the effect of advection. Indeed, advection is expected to become important at short times and for values of w_i close to unity. To make this clear, we define the Péclet number of the problem as the coefficient of the advection term in (4.10), namely $\Delta w_i \, Sh \, \rho/\rho_w = \rho v_y/h^* = (w|_{z=0} - w_{eq})\rho/\rho_w$. Notice that in our problem, the Péclet number is nothing more than the Sherwood number with a coefficient that modulates the importance of the initial water concentration. However, we find it useful

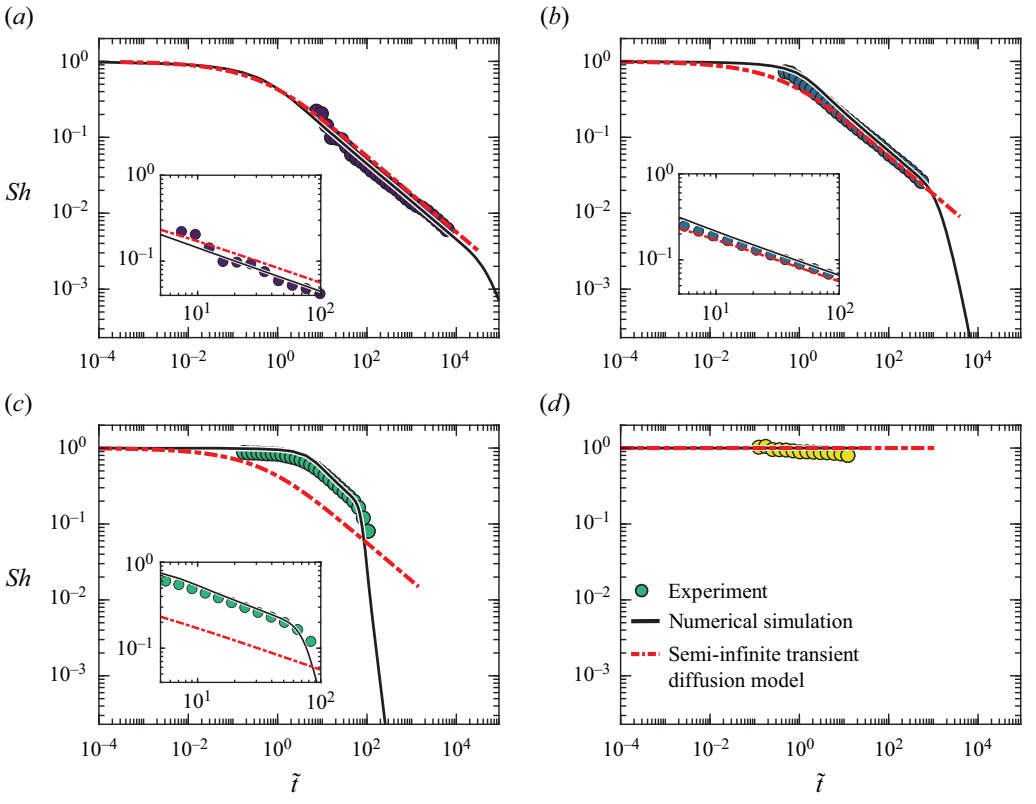

Figure 4. (*a–d*) Comparisons of the normalised evaporation rates (Sherwood number *Sh*) against normalised time ($\tilde{t}$) obtained from the experiments (discrete data points) and the numerical simulations (continuous lines) with theoretical values (dashed lines) obtained using the semi-infinite transient diffusion model (4.18), for different initial weight fractions of water $w_i = 0.2, 0.6, 0.9, 1.0$, respectively. Notice that in the $w_i = 1.0$ case in (*d*), the theoretical curve corresponds to $Sh = 1$, not that given by (4.18). Note also that all the theoretical curves for $w_i < 1.0$ are the same, as (4.18) does not take into account w_i. Insets highlight the comparisons between the experiments, the numerical simulations and the simplified analytical modelling.

to work with this quantity in order to evaluate the effect of advection. This Péclet number is plotted in figure 5, where we can see that it becomes of order unity during the first stage of the evaporation process for $w_i \gtrsim 0.6$.

To predict quantitatively the evaporation dynamics including the effect of advection, we propose an improvement over our simplistic analytical model. We will first develop an asymptotic solution, valid formally in the limit $\tilde{t} \gg 1$, and then present an approximate expression for *Sh* that converges uniformly to the asymptotic solution for $\tilde{t} \gg 1$ and to $Sh \approx 1$ for $\tilde{t} \ll 1$.

We start from the problem formulated in (4.10) and (4.11), with $\tilde{L} \to \infty$. In order to make the problem tractable, we assume that the mixture's density is constant and equal to the initial one, $\rho = \rho(w_i)$. The transport problem (4.10) with advection becomes

$$\frac{\partial \tilde{w}}{\partial \tilde{t}} - \Delta w_i \, Sh \, \frac{\rho}{\rho_w} \frac{\partial \tilde{w}}{\partial \tilde{z}} = \frac{\partial^2 \tilde{w}}{\partial \tilde{z}^2}, \tag{4.19}$$

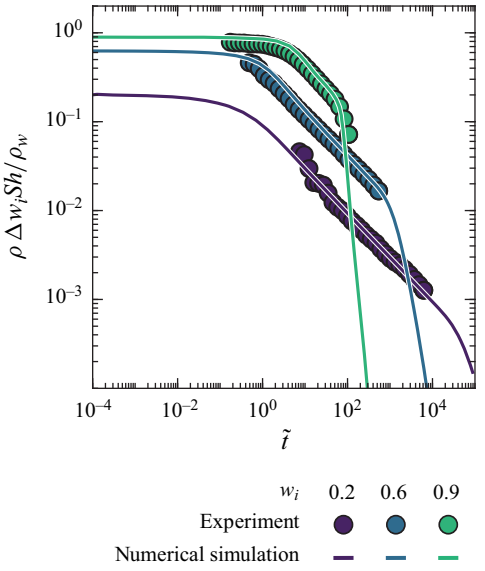

Figure 5. Plots showing the variation of the Péclet number $\rho\,\Delta w_i\,Sh/\rho_w$ with the normalised time $\tilde{t}$ for three different initial water concentrations, $w_i = 0.2$, 0.6 and 0.9.

with one initial and two boundary conditions (4.11), namely

$$\left.\begin{aligned} \tilde{w} = 0 \quad &\text{at } \tilde{t} = 0, \\ \frac{\partial \tilde{w}}{\partial \tilde{z}} = 0 \quad &\text{at } \tilde{z} \to \infty, \\ \frac{\partial \tilde{w}}{\partial \tilde{z}} - \left(1 - \Delta w_i \frac{\rho}{\rho_w} Sh\right)\tilde{w} + 1 - \frac{\rho}{\rho_w} w_i\, Sh = 0 \quad &\text{at } \tilde{z} = 0, \end{aligned}\right\} \tag{4.20}$$

and with the Sherwood number Sh (the water evaporation rate at the interface) given by (4.12),

$$Sh = 1 - \tilde{w}(\tilde{z} = 0, \tilde{t}). \tag{4.21}$$

4.2.1. *Asymptotic solution*

We will now look for solutions at long times. Inspired by both experiments and numerical simulations, we investigate solutions where

$$Sh = A\tilde{t}^{-\lambda}, \tag{4.22}$$

with $\lambda > 0$. Further, since at long times we expect $\tilde{w}$ to approach unity everywhere, we propose the following change of variables:

$$W = 1 - \tilde{w} - Sh. \tag{4.23}$$

Thus $W \to 0$ as $\tilde{w} \to 1$ and $Sh \to 0$, i.e. at long times. Reformulating the problem in terms of the new variable and neglecting terms of $\mathcal{O}(Sh^2)$, (4.19)–(4.21) can be rewritten

as

$$\frac{\mathrm{d}\,Sh}{\mathrm{d}\tilde{t}} + \frac{\partial W}{\partial \tilde{t}} - \Delta w_i \frac{\rho}{\rho_w} Sh \frac{\partial W}{\partial \tilde{z}} = \frac{\partial^2 W}{\partial \tilde{z}^2}, \tag{4.24}$$

$$W = 1 - Sh \quad \text{at } \tilde{t} = 0, \tag{4.25}$$

$$\frac{\partial W}{\partial \tilde{z}} = 0 \quad \text{at } \tilde{z} \to \infty, \tag{4.26}$$

$$-\frac{\partial W}{\partial \tilde{z}} + Sh\left(1 + w_{eq}\frac{\rho}{\rho_w}\right) = 0 \quad \text{at } \tilde{z} = 0, \tag{4.27}$$

$$W(\tilde{z} = 0, t) = 0. \tag{4.28}$$

We seek self-similar solutions of the type $W(\tilde{z}, \tilde{t}) = F(\eta)$, with $\eta = \tilde{z}/\tilde{t}^{\lambda}$, in the limit $\tilde{t} \gg 1$. For such a self-similar solution to exist, the exponent λ of $\tilde{t}$ in the self-similar variable η must be the same as that in the definition of Sh by virtue of (4.27). Indeed, $\partial W/\partial \tilde{z} = F'\tilde{t}^{-\lambda}$. So if the time exponent in Sh and η were different, then (4.27) could not be made self-similar.

Substituting the proposed ansatz into (4.24), we get

$$-\lambda A\tilde{t}^{-\lambda-1} - \lambda\eta\tilde{t}^{-1}F' - \Delta w_i \frac{\rho}{\rho_w} A\tilde{t}^{-2\lambda}F' = \tilde{t}^{-2\lambda}F''. \tag{4.29}$$

For $\tilde{t} \gg 1$, the first term is always negligible compared to the second one, since $\lambda > 0$. Then, balancing the second term with the last two terms, we obtain that the equation becomes self-similar if $\lambda = 1/2$, as expected from the experiments and the simulations, resulting in

$$-\left(\frac{1}{2}\eta + A\,\Delta w_i \frac{\rho}{\rho_w}\right)F' = F''. \tag{4.30}$$

This differential equation can be solved with the boundary conditions $F(0) = 0$ (from (4.28)) and $F'(0) = A$ (from (4.27)) to yield

$$F(\eta) = -\sqrt{\pi}A\left(1 + w_{eq}\frac{\rho}{\rho_w}\right)\exp\left(A^2\,\Delta w_i^2\left(\frac{\rho}{\rho_w}\right)^2\right) \times \left(\operatorname{erf}\left(A\,\Delta w_i \frac{\rho}{\rho_w}\right) - \operatorname{erf}\left(A\,\Delta w_i \frac{\rho}{\rho_w} + \frac{\eta}{2}\right)\right). \tag{4.31}$$

Finally, an additional condition is needed to determine the value of A. This condition stems from the behaviour of W far away from the evaporation boundary $\tilde{z} = 0$, where $W \to 1$ (from (4.25) while neglecting $Sh \ll 1$ against unity). Introducing this condition into (4.31), we finally get

$$\sqrt{\pi}A\left(1 + w_{eq}\frac{\rho}{\rho_w}\right)\exp\left(A^2\,\Delta w_i^2\left(\frac{\rho}{\rho_w}\right)^2\right)\operatorname{erfc}\left(A\,\Delta w_i \frac{\rho}{\rho_w}\right) - 1 = 0. \tag{4.32}$$

The value of A can be evaluated numerically. Plotting A against w_i, we see that A grows monotonically with the initial water concentration, recovering the diffusion-driven asymptotic solution $A = 1/\sqrt{\pi}$ for $w_i \ll 1$ (if the additional assumption that $w_{eq} = 0$ is made; figure 6). This means that the higher the initial concentration of water w_i, the greater the advective enhancement of mass transfer compared to pure diffusion.

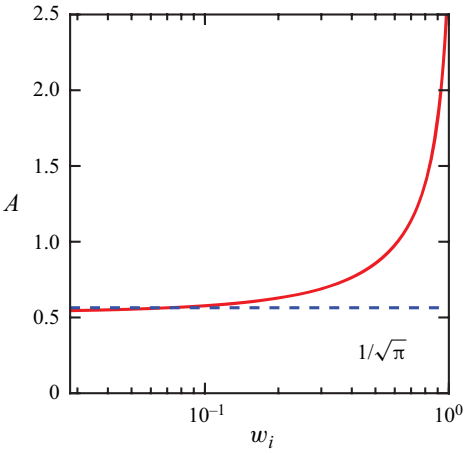

Figure 6. Coefficient A in $Sh = A\tilde{t}^{-1/2}$, obtained by solving (4.32) numerically, as a function of the initial water concentration. At low initial water concentrations, and under the assumption that $w_{eq} \approx 0$, we recover the pure diffusion regime, $A = 1/\sqrt{\pi}$ (blue dashed line). For large water concentrations, A grows unbounded, indicating that the regime $Sh \sim \tilde{t}^{-1/2}$ is never reached, as $Sh = 1$ in this limit.

4.2.2. *Uniform approximation*

For practical applications, it is desirable to have an approximate expression that converges to the asymptotic solutions in the limits $t \ll 1$ ($Sh \approx 1$) and $t \gg 1$ ($Sh \approx A\tilde{t}^{-1/2}$). To this end, we notice that the exact solution for the problem without advection,

$$Sh = \exp\left(\tilde{t}\right) \operatorname{erfc}\left(\sqrt{\tilde{t}}\right), \tag{4.33}$$

captures the behaviour of the numerical solution with advection, except that the prefactor of the equation $Sh \sim \tilde{t}^{-1/2}$ in (4.33) at $\tilde{t} \gg 1$ is $1/\sqrt{\pi}$, instead of A (as in (4.22)). Thus we propose the following expression to approximate the full numerical solution uniformly at all times:

$$Sh = \exp\left(\frac{\tilde{t}}{\pi A^2}\right) \operatorname{erfc}\left(\sqrt{\frac{\tilde{t}}{\pi A^2}}\right). \tag{4.34}$$

We observe that this approximation reproduces much more successfully the numerical simulations than the solution without advection, as shown in figure 7.

To conclude this subsection, we point out that another uniform approximation for computing the Sherwood number Sh, similar to (4.34), can be obtained by solving the simplified problem (4.19)–(4.20) analytically considering advection as being quasi-constant. For completeness, this solution is described in Appendix E. The fact that treating advection as quasi-constant yields an expression that works fairly well is interesting, as it points out that advection is important mostly when it is nearly constant, that is, at short times (see figure 5). This makes sense, since it is at this stage when the Péclet number reaches the largest value. This idea could be useful in pursuing further analytical approaches for similar problems.

4.3. *Transient diffusion model with finite-length effects*

The models described in §§ 4.1 and 4.2 can explain faithfully both $Sh = 1$ and $Sh \sim \tilde{t}^{-1/2}$ behaviours seen in the experiments and the simulations. However, we are yet to explain

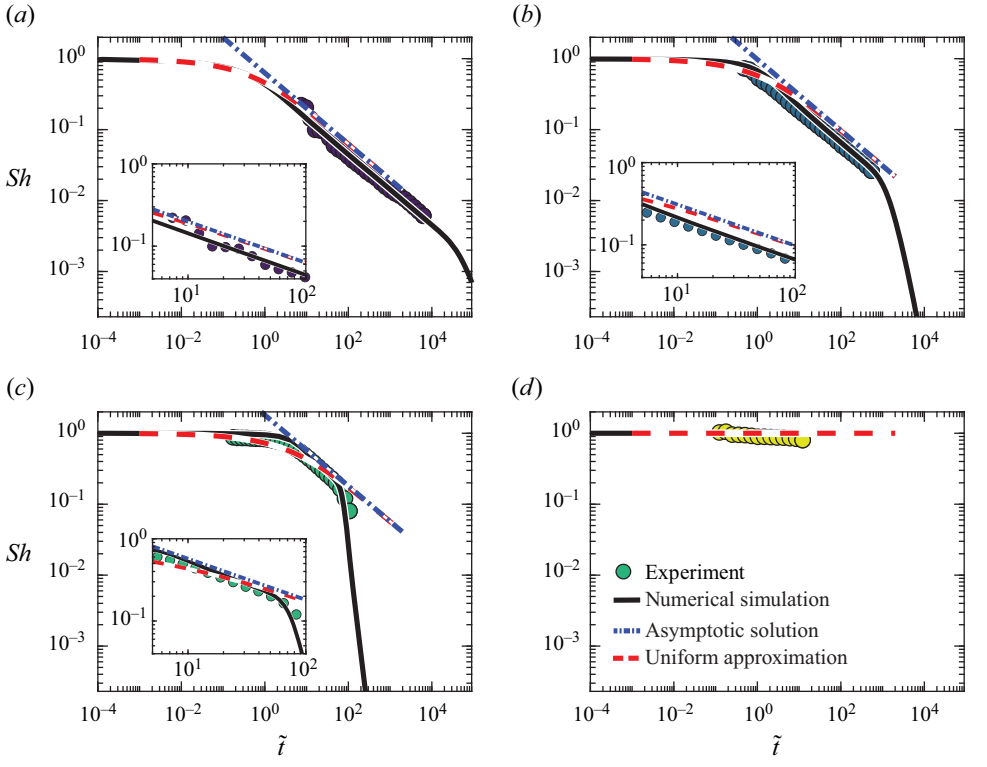

Figure 7. Variation of the normalised evaporation rates (Sherwood number Sh) with normalised time ($\tilde{t}$) obtained from the experiments (discrete data points), the numerical simulations (continuous lines), the asymptotic solution for long times (dash–dotted lines) and the approximate expression ((4.34), dashed lines), for different initial weight fractions of water w_i: (*a*) $w_i = 0.2$, (*b*) $w_i = 0.6$, (*c*) $w_i = 0.9$ and (*d*) $w_i = 1.0$. Insets highlight the comparisons between the experiments, the numerical simulations and the simplified analytical modelling.

the sharp deviation from $Sh \sim \tilde{t}^{-1/2}$ seen for very late times in the simulations at $w_i = 0.6$ and 0.9 (figures 7*b*,*c*). To this end, we turn our attention to the semi-infinite assumption.

For the semi-infinite assumption to hold, the penetration depth of the diffusion front $\delta(t) = \sqrt{Dt}$ should be much smaller than the length of the liquid column $L(t)$. We plot the variation of δ/L ($= \sqrt{Dt}/L$) with $\tilde{t}$ as obtained from the experiments and the numerical simulations in figure 8 for different w_i. It can be observed that for $w_i = 0.9$, $\delta/L = 1$ at $\tilde{t} \approx 60$, which agrees approximately with the time when the slope of $Sh(\tilde{t})$ starts to deviate from $Sh \sim \tilde{t}^{-1/2}$ in figure 7(*c*). The same holds true for $w_i = 0.6$ at $\tilde{t} \approx 10^3$ (figure 7*b*). Thus we conclude that although the semi-infinite assumption holds at early times, finite-length effects should be included at later times for $w_i = 0.6$ and 0.9 in order to capture accurately the physics of the problem.

We show in this subsection that this is an effect of the finite length of the capillary, which becomes relevant at long times. To include the effects of the finite length, we use the original boundary conditions of (3.3).

We will first check how the three terms in the governing equation (4.10), reproduced here for convenience, compare with each other for the late times when the finite-length

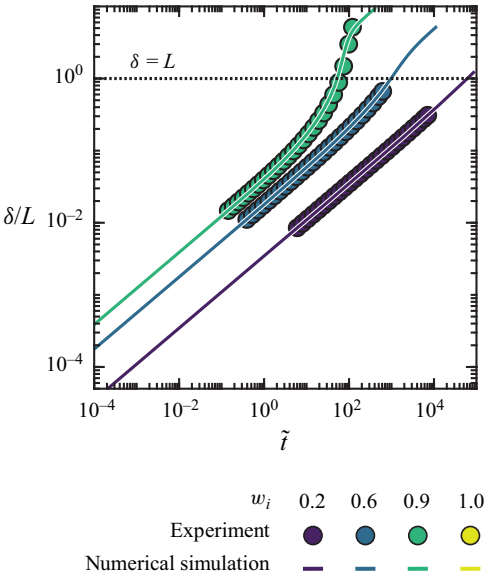

Figure 8. Variation of the penetration depth δ (normalised by the length L of the liquid column) with the normalised time $\tilde{t}$. Discrete data points are based on the experiments, and continuous lines are based on the numerical simulations. The dotted line at $\delta/L = 1$ indicates when the penetration depth is equal to the size of the liquid column. The penetration depth is defined as $\delta(t) = \sqrt{Dt}$.

effects start playing a role:

$$\frac{\partial \tilde{w}}{\partial \tilde{t}} - \frac{\rho\, \Delta w_i}{\rho_w}\, Sh\, \frac{\partial \tilde{w}}{\partial \tilde{z}} = \frac{\partial^2 \tilde{w}}{\partial \tilde{z}^2}. \tag{4.35}$$

When the boundary layer becomes of the order of the length of the domain, $\delta \sim L$, the first and second spatial derivatives in (4.35) scale as $\Delta\tilde{w}/\tilde{L}$ and $\Delta\tilde{w}/\tilde{L}^2$, respectively. For $w_i < 1$, the volume occupied by water at long times is small compared to that occupied by glycerol, so $\tilde{L}$ tends asymptotically to a constant as the total liquid volume changes very slowly. This means that the orders of magnitude of the first and second spatial derivatives differ by a constant factor $\tilde{L}$. In this situation, since the prefactor of the advective term goes to zero as $Sh \to 0$, the advective term is going to be a factor of Sh smaller than the diffusive one and can be neglected. Thus we formulate a quasi-constant-length transient diffusion model valid for $Sh \ll 1$.

The governing equations and the initial and boundary conditions ((4.10)–(4.12)) can now be written as

$$\frac{\partial \tilde{w}}{\partial \tilde{t}} = \frac{\partial^2 \tilde{w}}{\partial \tilde{z}^2}, \tag{4.36}$$

$$\left.\begin{aligned} \tilde{w} &= 0 \quad \text{at } \tilde{t} = 0, \\ \frac{\partial \tilde{w}}{\partial \tilde{z}} &= 0 \quad \text{at } \tilde{z} = \tilde{L}, \\ \frac{\partial \tilde{w}}{\partial \tilde{z}} &= \tilde{w} - 1 \quad \text{at } \tilde{z} = 0, \end{aligned}\right\} \tag{4.37}$$

$$Sh = 1 - \tilde{w}(\tilde{z} = 0, \tilde{t}). \tag{4.38}$$

The solution of this system of equations is given by (Crank 1975)

$$\tilde{w}(\tilde{z},\tilde{t},\tilde{L}) = 1 - \sum_{n=1}^{\infty} \frac{2\tilde{L}\cos\left(\lambda_n\left(1-\tilde{z}/\tilde{L}\right)\right)\exp\left(-\lambda_n^2\tilde{t}/\tilde{L}^2\right)}{\left(\lambda_n^2+\tilde{L}^2+\tilde{L}\right)\cos(\lambda_n)}, \tag{4.39}$$

$$Sh = 1 - \tilde{w}(\tilde{z}=0,\tilde{t}) = \sum_{n=1}^{\infty} \frac{2\tilde{L}\exp\left(-\lambda_n^2\tilde{t}/\tilde{L}^2\right)}{\lambda_n^2+\tilde{L}^2+\tilde{L}}, \tag{4.40}$$

where λ_n is the nth root of the equation $\lambda\tan(\lambda) = \tilde{L}$. Combining (4.9) and (4.40), the velocity of the top interface can now be written as

$$\frac{\mathrm{d}L}{\mathrm{d}t} = v_y = \frac{h^*\,\Delta w_i}{\rho_w}\sum_{n=1}^{\infty} \frac{2\tilde{L}\exp\left(-\lambda_n^2\tilde{t}/\tilde{L}^2\right)}{\lambda_n^2+\tilde{L}^2+\tilde{L}}. \tag{4.41}$$

Equation (4.41) is integrated in time using the built-in Matlab function `ode45` (which implements an adaptive-time-step Runge–Kutta algorithm of fourth order) to obtain $L(t)$ and subsequently the variation of Sh with $\tilde{t}$ (figure 9*c*). For $\tilde{t} \gg 1$, v_y can be approximated by the first term in the series:

$$v_y = \frac{h^*\,\Delta w_i}{\rho_w}\,\frac{2\tilde{L}\,\exp\left(-\beta_1^2\tilde{t}/\tilde{L}^2\right)}{\beta_1^2+\tilde{L}^2+\tilde{L}}. \tag{4.42}$$

When the changes in the length L of the liquid column are slow, the velocity decreases exponentially with time (as per (4.42)), thus correctly predicting the late-time $Sh(\tilde{t})$ behaviour of $w_i = 0.9$ in the simulations (figure 9*c*). Note that observing this regime experimentally is complicated from the practical point of view, due to the very small velocities associated with it. Although we can observe it easily in the numerical simulations, we are able to see the beginning of this regime in the experiments only for the most favourable case, $w_i = 0.9$, for which this regime appears at velocities of the order of less than a micron per second (see figure 3). In conclusion, this model captures successfully the deviation from $Sh \sim \tilde{t}^{1/2}$ due to the finite-length effects.

5. Conclusions and outlook

In this work, we have studied the evaporation of aqueous glycerol solutions in cylindrical capillaries having a circular cross-section. We characterised the drying behaviour in terms of a normalised mass transfer rate (Sherwood number Sh) and a normalised time $\tilde{t}$. Our experiments demonstrate quantitatively how the addition of glycerol reduces the evaporation rate of water. The corresponding direct numerical simulations indicate that modelling the system as a one-dimensional advection–diffusion mass transfer problem with composition-dependent properties can reproduce quantitatively the evaporation behaviour observed in the experiments. The evaporation of water shows three main regimes: (i) $Sh = 1$, (ii) $Sh \sim 1/\sqrt{\tilde{t}}$ and (iii) $Sh \sim \exp(-\tilde{t})$. We describe the physical origins of these regimes using a one-dimensional simplistic analytical model with constant material properties and a linearised composition-dependent activity of water.

Modelling the system as a problem of pure diffusion in a semi-infinite medium reproduces $Sh = 1$ and $Sh \sim 1/\sqrt{\tilde{t}}$ as the early-time and late-time behaviours, respectively.

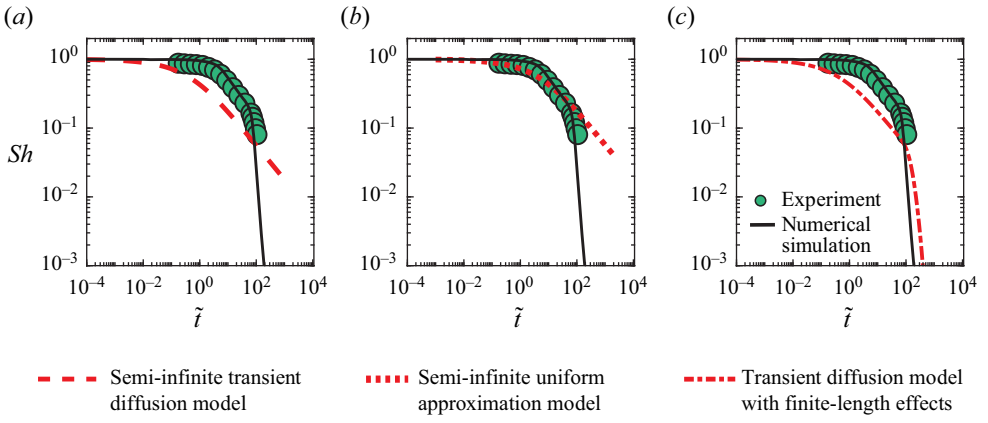

Figure 9. Plots comparing the normalised evaporation rates (Sherwood number Sh) versus normalised time ($\tilde{t}$) obtained from the experiments (discrete data points) and the numerical simulations (continuous lines) with the theoretical values obtained using (*a*) the semi-infinite transient diffusion model (dashed line), (*b*) the semi-infinite uniform approximation model (dotted line) and (*c*) the transient diffusion model with finite-length effects (dash–dotted line) for an initial weight fraction of water $w_i = 0.9$.

In the early time limit, $Sh = 1$ corresponds to a rapid replenishment of water at the evaporating interface, leading to a constant evaporation rate and constant interfacial concentration of water. In the late-time regime, replenishment of the interfacial concentration of water is limited by diffusion, leading to the classical diffusion-like $Sh \sim 1/\sqrt{\tilde{t}}$ behaviour.

However, we also show that even if the pure diffusion model captures the scaling relations of $Sh(\tilde{t})$ correctly, advective replenishment of water needs to be considered for more precise prediction of the evaporation rates. A Péclet number defined as $\Delta w_i\, Sh\, \rho/\rho_w = \rho v_y/h^* = (w|_{z=0} - w_{eq})\rho/\rho_w$ (the coefficient of the advective term in (4.10)) is the relevant parameter dictating the importance of advection. Thus advection is small when the interfacial concentration of water $w|_{z=0}$ is close to the equilibrium concentration w_{eq}, and high otherwise.

Finally, we show that as the diffusive penetration depth $\delta = \sqrt{Dt}$ increases and the length $L(t)$ of the system decreases, they can become comparable in magnitude. In such a scenario, the semi-infinite approximations hold only as long as the late-time behaviour is modified to $Sh \sim \exp(-\tilde{t})$. This change in the evaporation regime essentially reflects the effect of the finite size of the liquid column.

Even though a model with constant material properties was used to describe the evaporation of a binary mixture, the spatio-temporal changes in properties such as the density and the diffusion coefficient affect the precise quantitative prediction of evaporation rates. The direct numerical simulations are devoid of these deficiencies. However, the simplified analytical models provide valuable insight into the essential physics of the system and can provide predictions for more complex liquid mixtures.

We also note that for predicting the evaporation rate, we have used the expression corresponding to that of a thin droplet on a substrate ($\theta_{drop} = 0^\circ$), giving excellent predictions that match the experimental observations. However, one can include corrections to the mass transfer coefficient h^* to account for the difference between the air–liquid interface of a droplet and the air–liquid interface at the mouth of a capillary tube (Li *et al.* 2019). Moreover, during evaporation, the shape of the lower interface changes ($\theta < 90^\circ$) until the meniscus depins. This change in the shape of the interface may also

require a small correction to h^*, and might explain the very small decrease in Sh seen in the experiments on pure water (figure 3*b*). However, further studies along the lines of D'Ambrosio *et al.* (2021) are required to confirm this hypothesis.

Finally, all measurements were limited to times during which the lower meniscus was pinned at the mouth of the capillary. When the lower meniscus depins and propagates into the capillary, the rate-limiting step of evaporation would change from three-dimensional vapour diffusion to one-dimensional vapour diffusion. In the case of a single-component liquid evaporating from a square capillary, there have been efforts to predict the time when the lower meniscus depins (Chauvet *et al.* 2010). Further studies are required to predict the same for multi-component liquids and capillaries of various geometries and configurations (e.g. inclination with respect to gravity). Nonetheless, in this study, we have shown that these kinds of phenomena may not be essential to predict, with a reasonable degree of accuracy, the mass transfer rate in a relatively complex system such as the one that we consider here.

The aforementioned results can also be applied directly to predict the evaporation of multi-component liquids from porous structures, which can be modelled as bundles of thin capillaries. Evaporation from capillaries can also help us to understand the evaporative behaviour of biological fluids (such as blood, saliva or liquids in respiratory droplets; Merhi *et al.* 2022; Seyfert *et al.* 2022) or novel liquid mixtures (for applications such as evaporative cooling and spray drying). Finally, studying evaporation from capillaries can also be useful in the case of inkjet printing, where the evaporation from the tip of the printing nozzle can lead to changes in the composition of the ink (Rump *et al.* 2023). Our model can provide insight into the changes in the composition at the nozzle tip for a given time scale and assist in choosing carefully the properties of the ink.

Supplementary movie. A supplementary movie is available at https://doi.org/10.1017/jfm.2024.122.

Acknowledgements. The authors thank A. Prosperetti for insightful discussions, and M. Bos, G.-W. Bruggert, D. van Gils and T. Zijlstra for their assistance with the fabrication of the controlled humidity chamber.

Funding. We acknowledge funding from an Industrial Partnership Programme of the Netherlands Organisation for Scientific Research (NWO), co-financed by Canon Production Printing B.V., University of Twente and Eindhoven University of Technology. D.L. acknowledges funding from the ERC advanced grant no. 740479-DDD. J.R.R. acknowledges funding from the Spanish MCIN/AEI/10.13039/501100011033 through grant no. PID2020-114945RB-C21. X.Z. acknowledges support from the Natural Sciences and Engineering Research Council of Canada (NSERC), Alberta Innovates and the Canada Research Chairs programme.

Declaration of interests. The authors report no conflict of interest.

Author ORCIDs.
Lijun Thayyil Raju https://orcid.org/0000-0002-2054-3884;
Christian Diddens https://orcid.org/0000-0003-2395-9911;
Javier Rodríguez-Rodríguez https://orcid.org/0000-0001-8181-138X;
Xuehua Zhang https://orcid.org/0000-0001-6093-5324;
Detlef Lohse https://orcid.org/0000-0003-4138-2255;
Uddalok Sen https://orcid.org/0000-0001-6355-7605.

Appendix A. Evaporation from the upper interface

The evaporative flux from the top interface is given by (Stefan 1873)

$$\frac{\mathrm{d}M''}{\mathrm{d}t} = \frac{D_{v,a}}{L}\,\frac{p}{RT}\ln\left(\frac{p-p_{w,L}}{p-p_{w,s}}\right), \tag{A1}$$

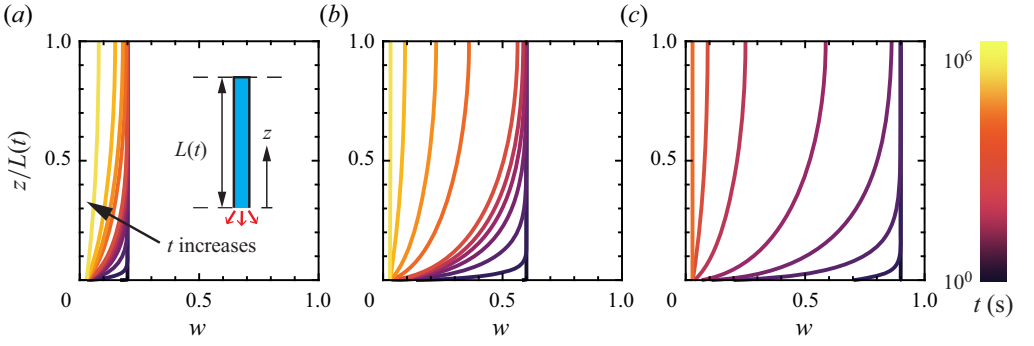

Figure 10. Axial distribution of the concentration field for three different initial concentrations: (*a*) $w_i = 0.2$, (*b*) $w_i = 0.6$ and (*c*) $w_i = 0.9$. The colours represent different time stamps: 1×10^0 s, 1×10^3 s, 1×10^4 s, 3×10^4 s, 5×10^4 s, 7×10^4 s, 1×10^5 s, 3×10^5 s, 5×10^5 s, 1×10^6 s and 3×10^6 s.

where p is the atmospheric pressure, $p_{w,s}$ is the partial pressure of water vapour at the surface of the upper meniscus, $p_{w,L}$ is the partial pressure of water vapour at the upper end of the capillary tube and L is the length of the capillary tube above the upper meniscus. Since $p_{w,s}$ is much smaller than p, the above expression can be simplified to

$$\frac{\mathrm{d}M''}{\mathrm{d}t} = \frac{D_{v,a}}{L}\left(\frac{p_{w,s}}{RT} - \frac{p_{w,L}}{RT}\right) = \frac{D_{v,a}}{L}\left(c_{w,s} - c_{w,L}\right). \tag{A2}$$

Thus the ratio of evaporative flux from the top interface to the bottom interface can be estimated as

$$\frac{\dfrac{\mathrm{d}M''_{top}}{\mathrm{d}t}}{\dfrac{\mathrm{d}M''_{bottom}}{\mathrm{d}t}} = \frac{\dfrac{D_{v,a}}{L}\left(c_{w,s} - c_{w,L}\right)_{top}}{\dfrac{4D_{v,a}}{\pi R}\left(c_{w,s} - c_{w,L}\right)_{bottom}}. \tag{A3}$$

Thus even if the top of the capillary is subjected to the same humidity as the bottom, the evaporation from the top is lower by a factor of $\pi R/4L = 0.005$. Hence the evaporation from the upper interface can be neglected.

Appendix B. Spatio-temporal changes in the concentration distribution within the capillary

We show in figure 10 snapshots of the concentration field inside the capillary for different initial water concentrations computed using the full numerical simulations described in § 3.2.

Appendix C. Linearisation of the water vapour concentration difference

The difference in concentration, $c_{w,s} - c_{w,\infty}$, of water vapour is a nonlinear function of the weight fraction of water w (figure 11, based on (3.6)). For our analytical model, we linearise $c_{w,s} - c_{w,\infty}$ between the initial concentration w_i and the equilibrium concentration w_{eq}. In figure 11, the corresponding coordinates are $(w_i, \Delta c_{w,i})$ and $(w_{eq}, 0)$,

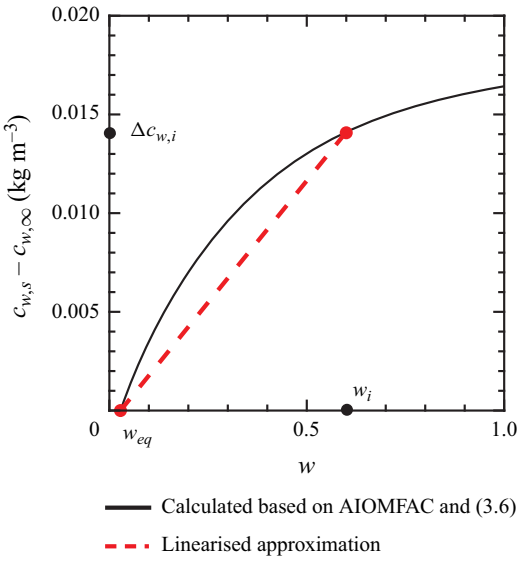

Figure 11. Difference in concentration of water vapour at the air–liquid interface and far away from the interface, at temperature 21 °C and relative humidity $H_r = 10\,\%$. The solid black line is calculated using AIOMFAC (Zuend *et al.* 2011) and (3.6). The dashed red line shows the linearised approximation used in (4.2) in the analytical model for $w_i = 0.6$. For our case, $w_{eq} = 0.028$.

where

$$\Delta c_{w,i} = c_{w,s} - c_{w,\infty} \tag{C1}$$

is the initial difference in the concentration of water vapour. From (3.6) and the definition $c_{w,\infty} = H_r c^o_{w,s}$, we get

$$\Delta c_{w,i} = a c^o_{w,s} - H_r c^o_{w,s} = x_i \psi_i c^o_{w,s} - H_r c^o_{w,s}. \tag{C2}$$

The equation for the line passing through these two points is given by

$$\frac{\left(c_{w,s} - c_{w,\infty}\right) - 0}{\left(x_i \psi_i c^o_{w,s} - H_r c^o_{w,s}\right) - 0} = \frac{w - w_{eq}}{w_i - w_{eq}}, \tag{C3}$$

which can be rewritten as

$$c_{w,s} - c_{w,\infty} = c^0_{w,s} \frac{x_i \psi_i - H_r}{\Delta w_i} (w - w_{eq}). \tag{C4}$$

Since (C4) applies at the boundary $z = 0$, we replace w in the right-hand side of (C4) with $w|_{z=0}$ to get (4.2).

Appendix D. Properties of water–glycerol mixtures

We include in this appendix plots showing the dependencies of the density and diffusivity of water–glycerol mixtures as functions of the mass fraction of water. These curves are the ones used in the numerical simulations described in § 3.2. For the analytical models described in § 4, we used constant values corresponding to the initial water concentration, which can also be read from figure 12.

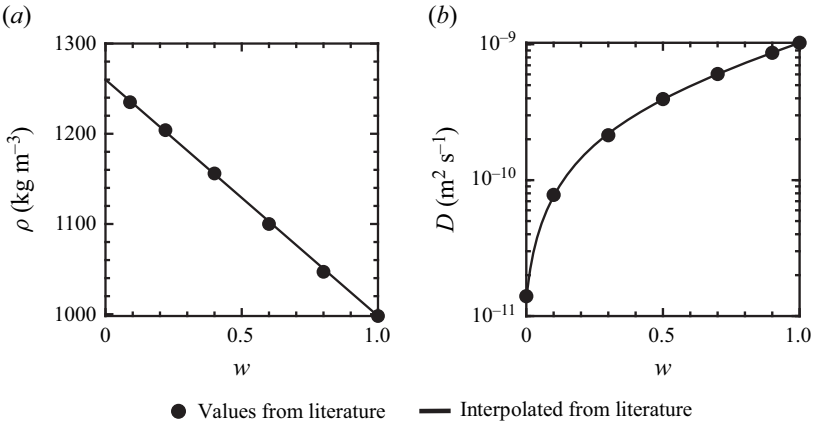

Figure 12. Material properties of the water–glycerol mixtures used in our direct numerical simulations: (*a*) density; (*b*) diffusivity. Data taken from D'Errico *et al.* (2004) and Takamura *et al.* (2012).

Appendix E. Simplified model with quasi-constant advection

In this appendix, we elaborate on the quasi-constant advection model referred to at the end of § 4.2. In addition to the approximations made at the beginning of § 4, we assume that the changes in velocity (and thus in *Sh*) are slow compared to the response of the concentration field, such that the velocity (and thus *Sh*) can be considered quasi-constant for the purpose of determining the concentration field. Thus we develop a transient diffusion model with quasi-constant advection.

We use the full form of (4.10) with the initial and boundary conditions given in (3.3), except that we modify the boundary condition at $\tilde{z} = \tilde{L}$:

$$\frac{\partial \tilde{w}}{\partial \tilde{t}} - \frac{\rho\, \Delta w_i\, Sh}{\rho_w} \frac{\partial \tilde{w}}{\partial \tilde{z}} = \frac{\partial^2 \tilde{w}}{\partial \tilde{z}^2}, \tag{E1}$$

$$\left.\begin{aligned} \tilde{w} &= 0 \quad \text{at } \tilde{t} = 0, \\ \frac{\partial \tilde{w}}{\partial \tilde{z}} &= 0 \quad \text{at } \tilde{z} \to \infty, \\ \frac{\partial \tilde{w}}{\partial \tilde{z}} - \left(1 - \frac{\rho\, \Delta w_i\, Sh}{\rho_w}\right) \tilde{w} + \left(1 - \frac{\rho w_i\, Sh}{\rho_w}\right) &= 0 \quad \text{at } \tilde{z} = 0. \end{aligned}\right\} \tag{E2}$$

We start with the Laplace transform of (E1) and (E2), to obtain

$$s\hat{w} - \tilde{w}(\tilde{t} = 0) - \alpha \frac{\partial \hat{w}}{\partial \tilde{z}} = \frac{\partial^2 \hat{w}}{\partial \tilde{z}^2}, \tag{E3}$$

$$\left.\begin{aligned} \frac{\partial \hat{w}}{\partial \tilde{z}} &= 0 \quad \text{at } \tilde{z} \to \infty, \\ \frac{\partial \hat{w}}{\partial \tilde{z}} - (1 - \alpha)\hat{w} + \frac{\beta}{s} &= 0 \quad \text{at } \tilde{z} = 0, \end{aligned}\right\} \tag{E4}$$

where $\hat{w}$ is the Laplace transform of $\tilde{w}$ and s is the variable in the Laplace domain. For the sake of brevity, we define

$$\alpha = \frac{\rho_w\, \Delta w\, Sh}{\rho} \tag{E5}$$

and

$$\beta = 1 - \frac{\rho_w w_i \, Sh}{\rho}. \tag{E6}$$

Solving this system of equations, we get

$$\hat{w} = \frac{-\beta}{s} \frac{1}{\dfrac{\alpha}{2} - 1 - \sqrt{s + \dfrac{\alpha^2}{4}}} \exp\left(-\frac{\alpha \tilde{z}}{2} - \tilde{z}\sqrt{\frac{\alpha^2}{4} + s} \right). \tag{E7}$$

Taking the inverse Laplace transform, we arrive at

$$L^{-1}\left(\hat{w}\right) = \tilde{w} = \beta \exp\left(\frac{-\alpha\tilde{z}}{2}\right) L^{-1}\left(\frac{1}{s} \frac{1}{\dfrac{\alpha}{2} - 1 - \sqrt{s + \dfrac{\alpha^2}{4}}} \exp\left(-\tilde{z}\sqrt{\frac{\alpha^2}{4} + s} \right) \right). \tag{E8}$$

Using the identity

$$L^{-1}[F(s - \zeta)] = \exp(\zeta)\, L^{-1} F(s) \tag{E9}$$

with $\zeta = -\alpha^2/4$, we obtain

$$\tilde{w} = \beta \exp\left(\frac{-\alpha\tilde{z}}{2}\right) \exp\left(\frac{-\alpha^2 \tilde{t}}{4}\right) L^{-1}\left(\frac{1}{s - \dfrac{\alpha^2}{4}} \frac{1}{1 - \dfrac{\alpha}{2} + \sqrt{s}} \exp\left(-\tilde{z}\sqrt{s}\right) \right). \tag{E10}$$

Further, we can write (van Genuchten & Alves 1982)

$$L^{-1}\left(\exp\left(\frac{-x\sqrt{s}}{(s - \mu^2)(\xi + s)} \right) \right) = \frac{C}{2(\mu + \xi)} - \frac{D}{2(\mu - \xi)} + E, \tag{E11}$$

where

$$C = \exp(\mu^2 t - \mu x) \operatorname{erfc}\left(\frac{x}{2\sqrt{t}} - \mu\sqrt{t} \right), \tag{E12}$$

$$D = \exp(\mu^2 t + \mu x) \operatorname{erfc}\left(\frac{x}{2\sqrt{t}} + \mu\sqrt{t} \right) \tag{E13}$$

and

$$E = \frac{\xi}{\mu^2 - \xi^2} \exp(\xi^2 t + \xi x) \operatorname{erfc}\left(\frac{x}{2\sqrt{t}} + \xi\sqrt{t} \right). \tag{E14}$$

With $\mu = \alpha/2$ and $\xi = 1 - \alpha/2$, we get

$$\tilde{w} = F + G + H, \tag{E15}$$

where

$$F = \frac{\beta}{2} \exp(-\alpha\tilde{z}) \operatorname{erfc}\left(\frac{\tilde{z}}{2\sqrt{\tilde{t}}} - \frac{\alpha\sqrt{\tilde{t}}}{2} \right), \tag{E16}$$

$$G = -\frac{\beta}{2(\alpha - 1)} \operatorname{erfc}\left(\frac{\tilde{z}}{2\sqrt{\tilde{t}}} + \frac{\alpha\sqrt{\tilde{t}}}{2} \right) \tag{E17}$$

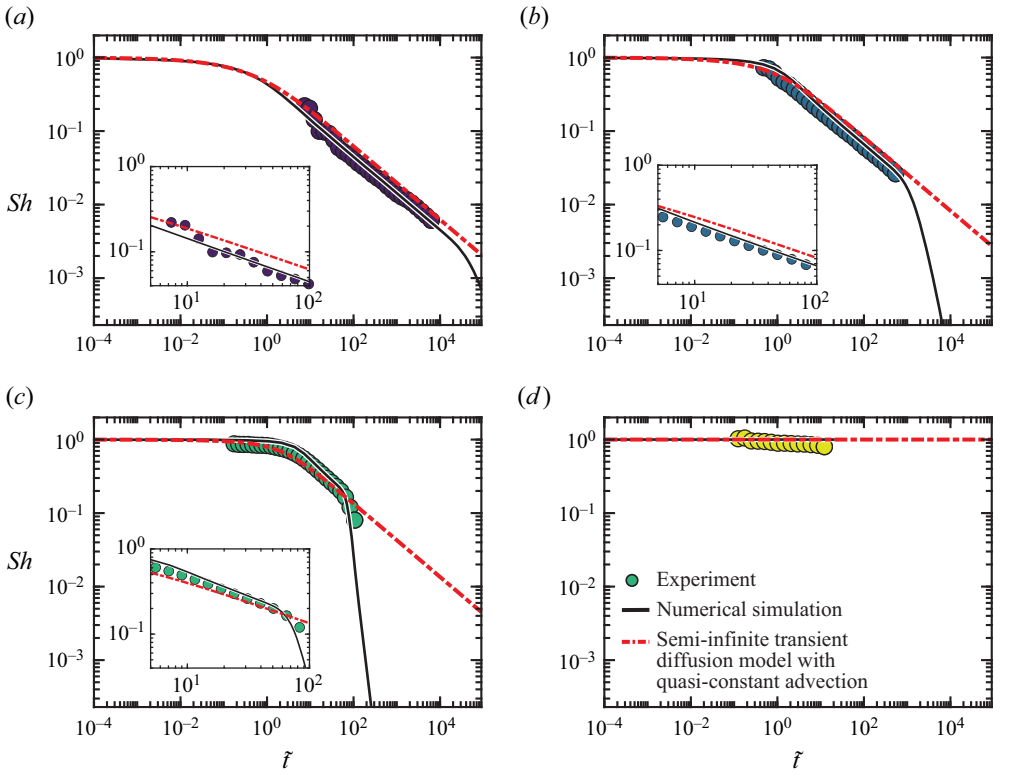

Figure 13. Variation of the normalised evaporation rates (Sherwood number Sh) with normalised time ($\tilde{t}$) obtained from the experiments (discrete data points) and the numerical simulations (continuous lines) with the theoretical values (dashed lines) obtained from the semi-infinite transient diffusion model with quasi-constant advection, for different initial weight fractions of water w_i: (*a*) $w_i = 0.2$, (*b*) $w_i = 0.6$, (*c*) $w_i = 0.9$ and (*d*) $w_i = 1.0$. Insets highlight the comparisons between the experiments, the numerical simulations and the simplified analytical modelling.

and

$$H = \frac{\beta}{2}\frac{2-\alpha}{\alpha-1}\exp\left((1-\alpha)\tilde{t}\right)\exp\left((1-\alpha)\tilde{z}\right)\operatorname{erfc}\left(\frac{\tilde{z}}{2\sqrt{\tilde{t}}}+\left(1-\frac{\alpha}{2}\right)\sqrt{\tilde{t}}\right). \tag{E18}$$

Finally, we use (4.12) along with (E15) to obtain an implicit equation for the Sherwood number:

$$\begin{aligned} Sh &= 1-\tilde{w}(\tilde{z}=0,\tilde{t}) \\ &= 1-\beta\left(1+\frac{\alpha}{2(1-\alpha)}\operatorname{erfc}\left(\frac{\alpha\sqrt{\tilde{t}}}{2}\right)-\frac{2-\alpha}{2(1-\alpha)}\exp((1-\alpha)\tilde{t})\operatorname{erfc}\left(\left(1-\frac{\alpha}{2}\right)\sqrt{\tilde{t}}\right)\right), \end{aligned} \tag{E19}$$

with

$$\alpha = \frac{\rho_w\,\Delta w\,Sh}{\rho} \tag{E20}$$

and

$$\beta = 1-\frac{\rho_w w_i\,Sh}{\rho}. \tag{E21}$$

Equation (E19) must be interpreted as an implicit algebraic equation to obtain Sh. The results of the quasi-constant advection with transient diffusion model (E19) are shown in figure 13, which indeed demonstrates a reasonably good quantitative agreement with the experiments and the direct numerical simulations. A close examination of (E19) reveals that in the early-time limit ($\tilde{t} \to 0$), we get $Sh \to 1$. Conversely, in the late-time limit ($\tilde{t} \gg 1$), we recover the diffusion-driven law $Sh \sim A\tilde{t}^{-1/2}$.

References

Abkarian, M., Nunes, J. & Stone, H.A. 2004 Colloidal crystallization and banding in a cylindrical geometry. *J. Am. Chem. Soc.* **126**, 5978–5979.

Bacchin, P., Leng, J. & Salmon, J.-B. 2022 Microfluidic evaporation, pervaporation, and osmosis: from passive pumping to solute concentration. *Chem. Rev.* **122**, 6938–6985.

Bennacer, R. & Sefiane, K. 2014 Vortices, dissipation and flow transition in volatile binary drops. *J. Fluid Mech.* **749**, 649–665.

Bourouiba, L. 2021 The fluid dynamics of disease transmission. *Annu. Rev. Fluid Mech.* **53**, 473–508.

Buffone, C. 2019 How external buoyancy controls the Marangoni convection for a volatile meniscus inside a pore. *Intl J. Therm. Sci.* **138**, 605–611.

Buffone, C. & Sefiane, K. 2003 Marangoni convection in capillary tubes filled with volatile liquids. In *International Conference on Nanochannels, Microchannels, and Minichannels, Proceedings of the ASME 2003 1st International Conference on Microchannels and Minichannels*, pp. 651–657. American Society of Mechanical Engineers.

Camassel, B., Sghaier, N., Prat, M. & Nasrallah, S.B. 2005 Evaporation in a capillary tube of square cross-section: application to ion transport. *Chem. Engng Sci.* **60**, 815–826.

Cecere, A., Buffone, C. & Savino, R. 2014 Self-induced Marangoni flow in evaporating alcoholic solutions. *Intl J. Heat Mass Transfer* **78**, 852–859.

Chauvet, F., Duru, P., Geoffroy, S. & Prat, M. 2009 Three periods of drying of a single square capillary tube. *Phys. Rev. Lett.* **103**, 124502.

Chauvet, F., Duru, P. & Prat, M. 2010 Depinning of evaporating liquid films in square capillary tubes: influence of corners' roundedness. *Phys. Fluids* **22**, 112113.

Chen, L., He, A., Zhao, J., Kang, Q., Li, Z.-Y., Carmeliet, J., Shikazono, N. & Tao, W.-Q. 2022 Pore-scale modeling of complex transport phenomena in porous media. *Prog. Energy Combust. Sci.* **88**, 100968.

Chen, X., Ye, H., Fan, X., Ren, T. & Zhang, G. 2016 A review of small heat pipes for electronics. *Appl. Therm. Engng* **96**, 1–17.

Christy, J.R.E., Hamamoto, Y. & Sefiane, K. 2011 Flow transition within an evaporating binary mixture sessile drop. *Phys. Rev. Lett.* **106**, 1–4.

Coussot, P. 2000 Scaling approach of the convective drying of a porous medium. *Eur. Phys. J.* B **15**, 557–566.

Crank, J. 1975 *The Mathematics of Diffusion*. Oxford University Press.

D'Ambrosio, H.-M., Colosimo, T., Duffy, B.R., Wilson, S.K., Yang, L., Bain, C.D. & Walker, D.E. 2021 Evaporation of a thin droplet in a shallow well: theory and experiment. *J. Fluid Mech.* **927**, A43.

Deegan, R.D., Bakajin, O., Dupont, T.F., Huber, G., Nagel, S.R. & Witten, T.A. 1997 Capillary flow as the cause of ring stains from dried liquid drops. *Nature* **389**, 827–829.

D'Errico, G., Ortona, O., Capuano, F. & Vitagliano, V. 2004 Diffusion coefficients for the binary system glycerol + water at 25 °C. A velocity correlation study. *J. Chem. Engng Data* **49**, 1665–1670.

Dhavaleswarapu, H.K., Chamarthy, P., Garimella, S.V. & Murthy, J.Y. 2007 Experimental investigation of steady buoyant-thermocapillary convection near an evaporating meniscus. *Phys. Fluids* **19**, 082103.

Dhavaleswarapu, H.K., Murthy, J.Y. & Garimella, S.V. 2012 Numerical investigation of an evaporating meniscus in a channel. *Intl J. Heat Mass Transfer* **55**, 915–924.

Diddens, C. 2017 Detailed finite element method modeling of evaporating multi-component droplets. *J. Comput. Phys.* **340**, 670–687.

Diddens, C., Tan, H., Lv, P., Versluis, M., Kuerten, J.G.M., Zhang, X. & Lohse, D. 2017 Evaporating pure, binary and ternary droplets: thermal effects and axial symmetry breaking. *J. Fluid Mech.* **823**, 470–497.

Duursma, G., Sefiane, K. & Clarke, J. 2008 Diffusion–evaporation studies of binary mixtures in capillary tubes. *Defect Diffus. Forum* **273–276**, 577–582.

ERBIL, H.Y. 2012 Evaporation of pure liquid sessile and spherical suspended drops: a review. *Adv. Colloid Interface Sci.* **170**, 67–86.

GAZZOLA, D., FRANCHI SCARSELLI, E. & GUERRIERI, R. 2009 3D visualization of convection patterns in lab-on-chip with open microfluidic outlet. *Microfluid. Nanofluid.* **7**, 659–668.

DE GENNES, P.G. 2001 Instabilities during the evaporation of a film: non-glassy polymer + volatile solvent. *Eur. Phys. J.* E **6**, 421–424.

VAN GENUCHTEN, M.T. & ALVES, W.J. 1982 Analytical solutions of the one-dimensional convective–dispersive solute transport equation. *Technical Bulletin* 1661. US Department of Agriculture, Agricultural Research Service.

GUERRIER, B., BOUCHARD, C., ALLAIN, C. & BÉNARD, C. 1998 Drying kinetics of polymer films. *AIChE J.* **44**, 791–798.

HE, F., WANG, Z., WANG, L., LI, J. & WANG, J. 2015 Effects of surfactant on capillary evaporation process with thick films. *Intl J. Heat Mass Transfer* **88**, 406–410.

HEIL, M. & HAZEL, A.L. 2006 *oomph-lib – An Object-Oriented Multi-Physics Finite-Element Library*. Lecture Notes in Computational Science and Engineering, vol. 53, pp. 19–49. Springer.

HOOIVELD, E., VAN DER KOOIJ, H., KISTERS, M., KODGER, T.E., SPRAKEL, J. & VAN DER GUCHT, J. 2023 *In-situ* and quantitative imaging of evaporation-induced stratification in binary suspensions. *J. Colloid Interface Sci.* **630**, 666–675.

HU, H. & LARSON, R.G. 2006 Marangoni effect reverses coffee-ring depositions. *J. Phys. Chem.* B **110**, 7090–7094.

HUISMAN, M., DIGARD, P., POON, W.C.K. & TITMUSS, S. 2023 The evaporation of concentrated polymer solutions is insensitive to relative humidity. *Phys. Rev. Lett.* **131**, 248102.

INCROPERA, F.P., DEWITT, D.P., BERGMAN, T.L. & LAVINE, A.S. 2007 *Fundamentals of Heat and Mass Transfer*. John Wiley & Sons.

KAMP, U., KITAEV, V., VON FREYMANN, G., OZIN, G.A. & MABURY, S.A. 2005 Colloidal crystal capillary columns – towards optical chromatography. *Adv. Mater.* **17**, 438–443.

KEITA, E., FAURE, P., RODTS, S., COUSSOT, P. & WEITZ, D.A. 2014 Evaporation from a capillary tube: experiment and modelisation. In *5th International Conference on Porous Media and Their Applications in Science, Engineering and Industry*. Engineering Conferences International.

KEITA, E., KOEHLER, S.A., FAURE, P., WEITZ, D.A. & COUSSOT, P. 2016 Drying kinetics driven by the shape of the air/water interface in a capillary channel. *Eur. Phys. J.* E **39**, 23.

LE DIZÈS CASTELL, R., PRAT, M., JABBARI FAROUJI, S. & SHAHIDZADEH, N. 2023 Is unidirectional drying in a round capillary always diffusive? *Langmuir*. **39**, 5462–5468.

LI, J., SHAN, L., MA, B., JIANG, X., SOLOMON, A., IYENGAR, M., PADILLA, J. & AGONAFER, D. 2019 Investigation of the confinement effect on the evaporation behavior of a droplet pinned on a micropillar structure. *J. Colloid Interface Sci.* **555**, 583–594.

LI, Y., DIDDENS, C., SEGERS, T., WIJSHOFF, H., VERSLUIS, M. & LOHSE, D. 2020 Rayleigh–Taylor instability by segregation in an evaporating multicomponent microdroplet. *J. Fluid Mech.* **899**, A22.

LOHSE, D. 2022 Fundamental fluid dynamics challenges in inkjet printing. *Annu. Rev. Fluid Mech.* **54**, 349–382.

LOHSE, D. & ZHANG, X. 2020 Physicochemical hydrodynamics of droplets out of equilibrium. *Nat. Rev. Phys.* **2**, 426–443.

LOPEZ DE LA CRUZ, R.A., DIDDENS, C., ZHANG, X. & LOHSE, D. 2021 Marangoni instability triggered by selective evaporation of a binary liquid inside a Hele-Shaw cell. *J. Fluid Mech.* **923**, A16.

MERHI, T., ATASI, O., COETSIER, C., LALANNE, B. & ROGER, K. 2022 Assessing suspension and infectivity times of virus-loaded aerosols involved in airborne transmission. *Proc. Natl Acad. Sci. USA* **119**, e2204593119.

MORRIS, D.H., *et al.* 2021 Mechanistic theory predicts the effects of temperature and humidity on inactivation of SARS-CoV-2 and other enveloped viruses. *eLife* **10**, e65902.

NAILLON, A., DURU, P., MARCOUX, M. & PRAT, M. 2015 Evaporation with sodium chloride crystallization in a capillary tube. *J. Cryst. Growth* **422**, 52–61.

NGUYEN, H.-T., BOUCHAUDY, A. & SALMON, J.-B. 2022 Microfluidic free interface diffusion: measurement of diffusion coefficients and evidence of interfacial-driven transport phenomena. *Phys. Fluids* **34**, 052008.

OKAZAKI, M., SHIODA, K., MASUDA, K. & TOEI, R. 1974 Drying mechanism of coated film of polymer solution. *J. Chem. Engng Japan* **7**, 99–105.

OKUZONO, T., OZAWA, K. & DOI, M. 2006 Simple model of skin formation caused by solvent evaporation in polymer solutions. *Phys. Rev. Lett.* **97**, 136103.

PALACIOS, J., HERNÁNDEZ, J., GÓMEZ, P., ZANZI, C. & LÓPEZ, J. 2012 On the impact of viscous drops onto dry smooth surfaces. *Exp. Fluids* **52**, 1449–1463.

PARK, K. & LEE, K.-S. 2003 Flow and heat transfer characteristics of the evaporating extended meniscus in a micro-capillary channel. *Intl J. Heat Mass Transfer* **46**, 4587–4594.

PICKNETT, R.G. & BEXON, R. 1977 The evaporation of sessile or pendant drops in still air. *J. Colloid Interface Sci.* **61**, 336–350.

POPOV, Y.O. 2005 Evaporative deposition patterns: spatial dimensions of the deposit. *Phys. Rev.* E **71**, 1–17.

POTASH, M. & WAYNER, P.C. 1972 Evaporation from a two-dimensional extended meniscus. *Intl J. Heat Mass Transfer* **15**, 1851–1863.

PRAT, M. 2002 Recent advances in pore-scale models for drying of porous media. *Chem. Engng J.* **86**, 153–164.

RANSOHOFF, T.C. & RADKE, C.J. 1988 Laminar flow of a wetting liquid along the corners of a predominantly gas-occupied noncircular pore. *J. Colloid Interface Sci.* **121**, 392–401.

ROGER, K. & CRASSOUS, J.J. 2021 How the interplay of molecular and colloidal scales controls drying of microgel dispersions. *Proc. Natl Acad. Sci. USA* **118**, e2105530118.

ROGER, K., LIEBI, M., HEIMDAL, J., PHAM, Q.D. & SPARR, E. 2016 Controlling water evaporation through self-assembly. *Proc. Natl Acad. Sci. USA* **113**, 10275–10280.

ROGER, K., SPARR, E. & WENNERSTRÖM, H. 2018 Evaporation, diffusion and self-assembly at drying interfaces. *Phys. Chem. Chem. Phys.* **20**, 10430–10438.

RUMP, M., SEN, U., JEURISSEN, R., REINTEN, H., VERSLUIS, M., LOHSE, D., DIDDENS, C. & SEGERS, T. 2023 Selective evaporation at the nozzle exit in piezoacoustic inkjet printing. *Phys. Rev. Appl.* **19**, 054056.

SALMON, J.-B., DOUMENC, F. & GUERRIER, B. 2017 Humidity-insensitive water evaporation from molecular complex fluids. *Phys. Rev.* E **96**, 032612.

SARKAR, A. & TIRUMKUDULU, M.S. 2009 Consolidation of charged colloids during drying. *Langmuir* **25**, 4945–4953.

SAURE, R., WAGNER, G.R. & SCHLÜNDER, E.-U. 1998 Drying of solvent-borne polymeric coatings: I. Modeling the drying process. *Surf. Coat. Technol.* **99**, 253–256.

SCHMIDT, G. & CHUNG, T. 1992 *Thermocapillary Flow About an Evaporating Meniscus*. American Institute of Aeronautics and Astronautics.

SEYFERT, C., RODRÍGUEZ-RODRÍGUEZ, J., LOHSE, D. & MARIN, A. 2022 Stability of respiratory-like droplets under evaporation. *Phys. Rev. Fluids* **7**, 023603.

SHAHIDZADEH-BONN, N., RAFAI, S., BONN, D. & WEGDAM, G. 2008 Salt crystallization during evaporation: impact of interfacial properties. *Langmuir* **24**, 8599–8605.

SHIN, S., JACOBI, I. & STONE, H.A. 2016 Bénard–Marangoni instability driven by moisture absorption. *Europhys. Lett.* **113**, 24002.

SOBAC, B. & BRUTIN, D. 2011 Triple-line behavior and wettability controlled by nanocoated substrates: influence on sessile drop evaporation. *Langmuir* **27**, 14999–15007.

SPARR, E. & WENNERSTRÖM, H. 2000 Diffusion through a responding lamellar liquid crystal: a model of molecular transport across stratum corneum. *Colloid Surf.* B **19**, 103–116.

STAUBER, J.M., WILSON, S.K., DUFFY, B.R. & SEFIANE, K. 2014 On the lifetimes of evaporating droplets. *J. Fluid Mech.* **744**, R2.

STEFAN, J. 1873 Versuche über die Verdampfung. *Sitzungsber. kais. Akad. Wiss. Wien. Math.* **68**, 385–423.

STEFAN, J. 1889 Über die Verdampfung und die Auflösung als Vorgänge der Diffusion. *Sitzungsber. kais. Akad. Wiss. Wien. Math.* **98**, 1418–1442.

SWANSON, L.W. & HERDT, G.C. 1992 Model of the evaporating meniscus in a capillary tube. *Trans. ASME J. Heat Transfer* **114**, 434–441.

TAKAMURA, K., FISCHER, H. & MORROW, N.R. 2012 Physical properties of aqueous glycerol solutions. *J. Petrol. Sci. Engng* **98–99**, 50–60.

TAN, H., DIDDENS, C., LV, P., KUERTEN, J.G.M., ZHANG, X. & LOHSE, D. 2016 Evaporation-triggered microdroplet nucleation and the four life phases of an evaporating Ouzo drop. *Proc. Natl Acad. Sci. USA* **113**, 8642–8647.

WANG, S., ZHOU, H., SUN, Z., XU, S., OUYANG, W. & WANG, L. 2020 Evolution of concentration and phase structure of colloidal suspensions in a two-ends-open tube during drying process. *Sci. Rep.* **10**, 9084.

WAYNER, P.C. & COCCIO, C.L. 1971 Heat and mass transfer in the vicinity of the triple interline of a meniscus. *AIChE J.* **17** (3), 569–574.

WAYNER, P.C., KAO, Y.K. & LACROIX, L.V. 1976 The interline heat-transfer coefficient of an evaporating wetting film. *Intl J. Heat Mass Transfer* **19**, 487–492.

YIOTIS, A.G., TSIMPANOGIANNIS, I.N., STUBOS, A.K. & YORTSOS, Y.C. 2007 Coupling between external and internal mass transfer during drying of a porous medium. *Water Resour. Res.* **43**, W06403.

ZHOU, L., ZHOU, S., DU, X. & YANG, Y. 2018 Heat transfer characteristics of a binary thin liquid film in a microchannel with constant heat flux boundary condition. *Intl J. Therm. Sci.* **134**, 612–621.

ZIMMERMANN, M., BENTLEY, S., SCHMID, H., HUNZIKER, P. & DELAMARCHE, E. 2005 Continuous flow in open microfluidics using controlled evaporation. *Lab on Chip* **5** (12), 1355–1359.

ZUEND, A., MARCOLLI, C., BOOTH, A.M., LIENHARD, D.M., SOONSIN, V., KRIEGER, U.K., TOPPING, D.O., MCFIGGANS, G., PETER, T. & SEINFELD, J.H. 2011 New and extended parameterization of the thermodynamic model AIOMFAC: calculation of activity coefficients for organic–inorganic mixtures containing carboxyl, hydroxyl, carbonyl, ether, ester, alkenyl, alkyl, and aromatic functional groups. *Atmos. Chem. Phys.* **11**, 9155–9206.